Monthly Notices
of the
ROYAL ASTRONOMICAL SOCIETY

MNRAS **431,** 2063–2079 (2013)
Advance Access publication 2013 March 22

doi:10.1093/mnras/stt225

The UV and X-ray activity of the M dwarfs within 10 pc of the Sun

B. Stelzer,[1]★ A. Marino,[2] G. Micela,[1] J. López-Santiago[3] and C. Liefke[4]

[1] *INAF - Osservatorio Astronomico di Palermo, Piazza del Parlamento 1, I-90134 Palermo, Italy*
[2] *Dipartimento di Fisica e Astronomia, G. Galilei, vicolo dell'Osservatorio 3, I-35122 Padova, Italy*
[3] *Departamento de Astrofísica y Ciencias de la Atmósfera, Facultad de Ciencias Físicas, Universidad Complutense de Madrid, E-28040 Madrid, Spain*
[4] *Zentrum für Astronomie der Universität Heidelberg, Mönchhofstrasse 12–14, D-69120 Heidelberg, Germany*

Accepted 2013 February 4. Received 2013 January 31; in original form 2012 November 15

ABSTRACT

M dwarfs are the most numerous stars in the Galaxy. They are characterized by strong magnetic activity. The ensuing high-energy emission is crucial for the evolution of their planets and the eventual presence of life on them. We systematically study the X-ray and ultraviolet emission of a subsample of M dwarfs from a recent proper-motion survey, selecting all M dwarfs within 10 pc to obtain a nearly volume-limited sample (∼90 per cent completeness). Archival *ROSAT*, *XMM–Newton* and *GALEX* data are combined with published spectroscopic studies of Hα emission and rotation to obtain a broad picture of stellar activity on M dwarfs. We make use of synthetic model spectra to determine the relative contributions of photospheric and chromospheric emission to the ultraviolet flux. We also analyse the same diagnostics for a comparison sample of young M dwarfs in the TW Hya association (∼10 Myr). We find that generally the emission in the *GALEX* bands is dominated by the chromosphere but the photospheric component is not negligible in early-M field dwarfs. The surface fluxes for the Hα, near-ultraviolet, far-ultraviolet and X-ray emission are connected via a power-law dependence. We present here for the first time such flux–flux relations involving broad-band ultraviolet emission for M dwarfs. Activity indices are defined as flux ratio between the activity diagnostic and the bolometric flux of the star in analogy to the Ca II $R'_{\rm HK}$ index. For given spectral type, these indices display a spread of 2–3 dex which is largest for M4 stars. Strikingly, at mid-M spectral types, the spread of rotation rates is also at its highest level. The mean activity index for fast rotators, likely representing the saturation level, decreases from X-rays over the *FUV* to the *NUV* band and Hα, i.e. the fractional radiation output increases with atmospheric height. The comparison to the ultraviolet and X-ray properties of TW Hya members shows a drop of nearly three orders of magnitude for the luminosity in these bands between ∼10 Myr and few Gyr age. A few young field dwarfs (<1 Gyr) in the 10-pc sample bridge the gap indicating that the drop in magnetic activity with age is a continuous process. The slope of the age decay is steeper for the X-ray than for the UV luminosity.

Key words: stars: activity – stars: chromospheres – stars: coronae – stars: late-type – ultraviolet: stars – X-rays: stars.

1 INTRODUCTION

Research on M dwarfs has become of central interest for astronomy, partly motivated by their importance as hosts of habitable planets (Tarter et al. 2007). Understanding the evolution of planets on M dwarfs and their potential for hosting life requires good knowledge of the stellar properties, and in particular of the phenomena related to magnetic activity. The fact that the habitable zone (HZ) of planets is closer to the star for M stars with respect to earlier spectral types implies that planets in the HZ of M stars receive enhanced high-energy radiation. The stellar emission from the ultraviolet (UV) to the X-ray regime has been recognized to (i) critically affect planet evolution and (ii) influence the chemistry in the planet atmospheres in a way that is crucial for life.

(i) X-ray (2–100 Å) and EUV (100–900 Å) radiation lead to heating and expansion of a hydrogen-rich planet atmosphere which may become unstable and evaporate (e.g. Lammer et al. 2003; Cecchi-Pestellini et al. 2009). Hydrodynamic models for the Earth thermosphere show that strong EUV radiation of the early Sun may have been able to induce atmospheric blow-off (Tian et al. 2008).

★ E-mail: stelzer@astropa.unipa.it

Published by Oxford University Press on behalf of the Royal Astronomical Society

The amount by which the planet mass is reduced over time by atmospheric escape clearly depends on the radiation input and its time evolution.

(ii) As a consequence of the exposure to strong and variable high-energy radiation from the host star the liquid–water HZs defined in Kasting, Whitmire & Reynolds (1993) may not necessarily be 'habitable'. The most biologically relevant high-energy emission is the near-UV range (∼2000–3000 Å). The appropriate amount of near-UV radiation for a HZ is confined between a minimum flux required for biochemical processes to take place and a maximum flux that prevents damage to biological systems (Buccino, Lemarchand & Mauas 2007). The far-UV ($<$2000 Å) is also important for photochemistry on exoplanets (Segura et al. 2005).

To date any quantitative evaluation of the evolution of the planets of M dwarfs and the possibility of the existence of life on them are hampered by the poorly constrained knowledge on the spectral energy distribution (SED) of the stellar high-energy radiation, the range of activity levels in M dwarfs and their evolution in time.

The coronal X-ray emission of nearby dMe (flare) stars has been intensively studied since the beginning of X-ray astronomy (Kahn et al. 1979; Schmitt & Rosso 1988). The relation between X-ray and bolometric luminosity, $L_{\rm x}/L_{\rm bol}$, was observed to saturate at a level of $\sim 10^{-3}$ for the most active stars with a downward spread of 2–3 dex. The strength of the X-ray emission has also been known for a while to be correlated with the equivalent width of Hα emission (Hawley, Gizis & Reid 1996), a tracer for magnetic activity in the chromosphere. M stars have little photospheric flux at UV and shorter wavelengths. Their UV emission is almost entirely produced in the chromosphere and transition region. In practice, very little is known on the UV properties of late-type stars in general and of M dwarfs in particular, as the UV is one of the least explored wavelength ranges in astronomy because of the strong interstellar absorption in this band.

As a result of our scarce knowledge on the UV emission of M dwarfs, for given planetary systems vastly different mass loss histories have been predicted depending on the assumptions of the X-ray and EUV flux (e.g. Lecavelier Des Etangs 2007; Penz & Micela 2008). Similarly, the chemistry of exoplanet atmospheres and their suitability for sustaining life is hard to determine without a good understanding of the incidence of stellar X-ray and UV radiation (e.g. Smith, Scalo & Wheeler 2004). The few available observations indicate that active M dwarfs outshine the Sun at far-UV wavelengths (Segura et al. 2005). However, these active flare stars are not representative for the whole class of M dwarfs, and virtually nothing is known about the UV emission of weakly active M dwarfs.

Until recently, the most extensive data base for stellar UV emission was the *IUE* archive (Byrne, Butler & Andrews 1980). As a result of the limitations of the available instrumentation, it remains unclear what are the relative contributions of the continuum and of the emission lines to the quiescent stellar UV radiation of M dwarfs. *Hubble Space Telescope* (*HST*) Space Telescope Imaging Spectrograph (STIS) studies of individual flare stars have revealed rich emission line spectra but could not detect any UV continuum emission (Pagano et al. 2000; Osten et al. 2006; Hawley et al. 2007). The *Galaxy Evolution Explorer* (*GALEX*) has opened a new opportunity for studying near- and far-UV emission of astrophysical sources (Martin et al. 2005). According to the above-mentioned spectroscopic studies, the *GALEX* far-UV band is dominated by emission lines formed in the transition region such as the Si IV$\lambda\lambda$1394, 1403 Å and C IV$\lambda\lambda$1546, 1550 Å doublets and He IIλ1640 Å. The *GALEX* near-UV band is dominated by iron lines. The by far strongest near-UV emission feature, Mg II $\lambda\lambda$2796, 2803 Å, is at the border of the *GALEX* near-UV band where filter transmission is low such that the major part of this emission feature is lost.

In spite of the fact that the *GALEX* satellite is dedicated to extragalactic astronomy, its large potential for stellar studies has already been demonstrated. In a serendipitous observation of the flare star GJ 3685 A, a large flare was observed in both the near-UV and the far-UV bands (Robinson et al. 2005). UV variability on other stars was discussed by Welsh et al. (2006, 2007). *GALEX* observations have also been proposed as a tool for identifying M stars in nearby clusters (Browne, Welsh & Wheatley 2009) and young associations (Rodriguez et al. 2011; Shkolnik et al. 2011). Finally, the UV activity of solar-type stars has been studied by Findeisen, Hillenbrand & Soderblom (2011) based on *GALEX* and Ca II H+K measurements.

In this paper we examine the UV/X-ray connection of the nearest M dwarfs by means of a statistical study combining UV measurements from *GALEX* with X-ray data from *ROSAT* and *XMM–Newton*. This data set is complemented by published spectroscopy yielding Hα emission and $v \sin i$. The latter is a proxy for the efficiency of the stellar dynamo that drives magnetic activity. The sample and the data are introduced in Section 2. The activity diagnostics derived from these data are described in Section 3. The characteristics of the sample's activity are presented in Section 4. Section 5 comprises a summary of the results and our conclusions.

2 SAMPLE AND CATALOGUE

Our sample is based on the *All-Sky Catalog of bright M dwarfs* published by (Lépine & Gaidos 2011, hereafter LG11). This catalogue comprises 8889 stars selected from the SUPERBLINK proper-motion survey using as criteria high proper motion ($\mu >$ 40 mas yr^{-1}), colours typical for M dwarfs ($V - J > 2.7$) and a magnitude cut-off ($J < 10$). Giant stars have been eliminated using cuts in absolute magnitude and reduced proper motion. We refer to LG11 for details.

We have selected all 163 stars from LG11 within 10 pc. Within this distance all stars in the catalogue have trigonometric parallaxes and the majority have an entry in the *Catalog of Nearby Stars*, CNS 3 (Gliese & Jahreiss 1995).

LG11 provide optical magnitudes from *Tycho*, optical photographic magnitudes from the USNO-B1.0 catalogue (Monet et al. 2003), and near-infrared (NIR) magnitudes from Two Micron All Sky Survey (2MASS) (Cutri et al. 2003). They also list X-ray counterparts from the *ROSAT* All Sky Survey (RASS) and far-UV and near-UV counterparts from *GALEX*. The positions used by LG11 are the International Celestial Reference System (ICRS) coordinates for the 2000.0 epoch and have been extrapolated from the *Hipparcos* catalogue where available (van Leeuwen 2007) and from 2 MASS for the remaining objects. This implies that due to the considerable proper motion of these nearby stars the cross-correlation with the RASS and *GALEX* catalogues is not complete even more so as relatively small match radii were used by LG11 (15 arcsec for the RASS and 5 arcsec for *GALEX*). We have matched the coordinates given by LG11 with various catalogues taking into account the proper motion. As the proper-motion correction of the coordinates depends on the observing date which is not known a priori this is a two-step procedure the details of which are given below. Briefly summarized, in the first step, we searched for counterparts in a given catalogue using a large match radius (of the order of 1 arcmin). Then we extracted the observing date for the identified counterparts; we calculated the expected coordinates at that date and repeated the cross-correlation with a smaller match radius corresponding to the positional precision of the instrument. All matches and table handling were performed with the Virtual Observatory tool TOPCAT (Taylor 2005).

2.1 Photometry

2.1.1 X-rays

We searched for X-ray counterparts to the M dwarfs using the RASS Bright Source Catalog (BSC), the RASS Faint Source Catalog (FSC), the *Second ROSAT Source Catalog of Pointed Observations* (2RXP), and the *XMM–Newton Serendipitous Source Catalog* released in 2010 (2XMMi-DR3).

The initial match radius for the RASS catalogues is 80 arcsec motivated by the maximum proper motion expected for any of our targets within the approximately 10 years between the RASS and the epoch 2000.0. The coordinates of all sample stars that present an RASS counterpart after this step are extrapolated back to 1990 Oct 1, representative for the observing date of the RASS which lasted from 1990 Aug to Dec. The subsequent refined cross-match is performed with a radius of 40 arcsec (Neuhäuser et al. 1995). With this procedure all 58 X-ray identifications provided by LG11 for the 163 sample stars were recovered. Moreover, an additional 24 X-ray counterparts not listed as X-ray sources in LG11 were identified this way in the RASS.

For the cross-correlation of the pointed X-ray catalogues, 2RXP and 2XMMi-DR3, we performed the proper-motion correction of the coordinates individually for each object and for the given observation date. For the rest, we proceeded in the same way as for the RASS. The final match radius for the 2RXP is again 40 arcsec as found to be appropriate for pointed PSPC observations by Stelzer & Neuhäuser (2001). This way we identified 24 of the 163 stars as pointed *ROSAT* sources. 16 of them were not listed as X-ray emitters by LG11 and nine of them are not detected in the RASS. The majority are located within 10 arcsec of the optical/NIR position and the maximum displacement is 25 arcsec.

In an analogous way, 11 stars are identified in the 2XMMi-DR3. Although we permitted a rather large match radius of 20 arcsec after the proper-motion correction all *XMM–Newton* counterparts are within 3 arcsec of the expected optical coordinates. For one star with two *XMM–Newton* identifications at similar separation from the optical source (∼2 arcsec) we retained the one from the observation with longer exposure time. Only two stars with *XMM–Newton* detection are not detected in any of the *ROSAT* catalogues. These two are actually one *XMM–Newton* source identified with two optical objects, PM I23318+1956 E + Wn (Gl 896 A+B).

To summarize, 93 of 163 M dwarfs within 10 pc have an X-ray counterpart, i.e. there are ≈57 per cent more identifications than presented by LG11.

2.1.2 Ultraviolet

GALEX performs imaging in two UV bands, far-UV (henceforth *FUV*; $\lambda_{\rm eff} = 1539$ Å, $\Delta\lambda = 1344 - 1786$ Å) and near-UV (henceforth *NUV*; $\lambda_{\rm eff} = 2316$ Å, $\Delta\lambda = 1771 - 2831$ Å) with a spatial resolution of 4.2 and 5.3 arcsec in the two bands, respectively. Three nested *GALEX* imaging surveys have been performed: the All-Sky Survey (AIS) covering a large fraction (∼85 per cent) of the high Galactic latitude ($\|b\| > 20°$) sky to $m_{\rm AB} \sim 21$ mag, the Medium Imaging Survey (MIS) reaching $m_{\rm AB} \sim 23$ mag on 1000 deg^2, and the Deep Imaging Survey (DIS) extending to $m_{\rm AB} \sim 25$ mag on 80 deg^2 (e.g. Bianchi 2009). These main surveys are complemented by guest investigator programmes.

The 10-pc sample was cross-correlated with the *GALEX* data distributed in the Data Release 6 (GR6), which has been homogeneously reduced and analysed by a dedicated software pipeline, available at the Mikulski Archive for Space Telescopes (MAST).[1]

In the first step of our cross-correlation procedure, we used the maximum possible match radius in MAST (60 arcsec). After the proper-motion correction for the *GALEX* observing dates extracted for our targets, we reduced the match radius to 10 arcsec for the final cross-correlation. Only sources having a distance from the centre of the field of view ≤50 arcmin were retained as generally the photometric quality is better in the central part of the field (Bianchi et al. 2011). In the case of multiple matches in the same observation, we retained the nearest source to the target. If the multiple matches were from different observations, they were assumed to be multiple observations of the same source. This yields *GALEX* counterparts to 72 of the 163 sample stars, of which all but one were observed in both *FUV* and *NUV*. All 71 stars observed in the *NUV* were detected while 49 of the 72 stars observed in the *FUV* were detected. Most of the stars (82 per cent) were observed in the AIS, 11 were observed in the MIS and only two in the DIS. 56 (∼34 per cent) of the remaining 91 stars of the sample do not fall in the area covered by *GALEX*.

We note that only 30 stars are listed as *NUV* and 54 listed as *FUV* sources in LG11. Analogous to the case of the X-ray sources, our significantly larger number of UV identifications is likely due to the fact that LG11 have not corrected for proper motion when cross-correlating catalogues.

2.2 Spectroscopic parameters

LG11 provide spectral types for all sample stars derived from the $V - J$ colour using a calibration based on SUPERBLINK stars that have a Sloan Digital Sky Survey (SDSS) spectrum. In their follow-up work of their proper-motion-selected catalogue, Lepine et al. (2012) checked that calibration for a spectroscopically confirmed part of the sample. They found that for stars with red colours this $V - J$ calibration tends to predict spectral types that are between 1 and 2 subclasses too cool. They redetermined the $V - J$ versus spectral type relationship by fitting a third-order polynomial to the observed distribution.

We adopted this updated calibration to compute the spectral types for all stars in the 10-pc sample from the $V - J$ colours given by LG11. We performed an independent literature search and found spectroscopically derived spectral types for all but two stars of the 10-pc sample. In particular, we have cross-matched our sample with the recent catalogue of rotation and activity in early-M stars by Reiners, Joshi & Goldman (2012), with Mohanty & Basri (2003) which comprises stars with spectral type M4 and later and with the Palomar/MSU survey by Reid, Hawley & Gizis (1995). These three catalogues together yield spectral types for 154 stars. Another seven have spectral types listed in Rojas-Ayala et al. (2012), Torres et al. (2006), Scholz et al. (1999) and Reid, Cruz & Allen (2007).

To obtain the effective temperature ($T_{\rm eff}$) from the spectral types we combined the temperature scales from Bessell (1991) and Mohanty & Basri (2003). These two scales span the full M spectral class. A comparison between the effective temperatures obtained from the spectroscopically determined spectral types with those from $V - J$ is shown in Fig. 1. The corrected $V - J$ versus spectral type relation presented by Lepine et al. (2012) is in good agreement

---

[1] http://galex.stsci.edu/casjobs

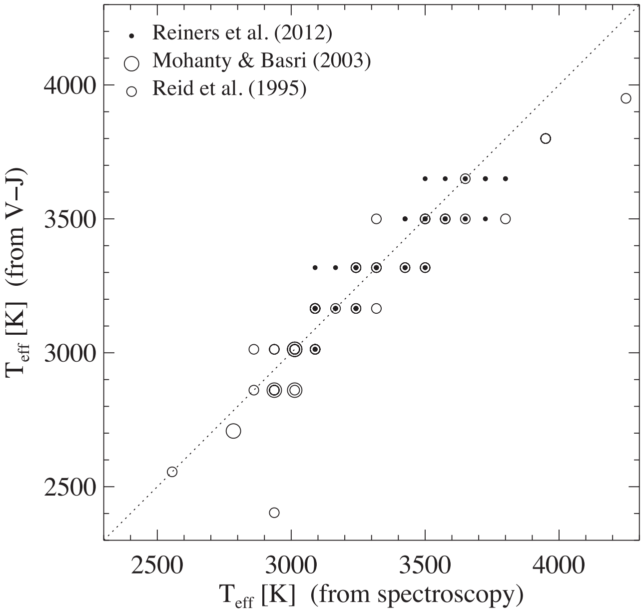

Figure 1. Comparison of the effective temperatures obtained from the $V-J$ versus spectral type calibration given by Lepine et al. (2012) and the spectral types from the spectroscopic literature. The adopted temperature scale is from Bessell (1991) and Mohanty & Basri (2003). Several of the 159 stars in this plot are at the same position. Omitted are only the two stars without spectroscopic spectral type determination and the two stars with spectral type cooler than M9 according to Lepine et al. (2012).

with the spectroscopically determined spectral types with few exceptions. These comprise also two stars for which the $V-J$ versus spectral type relation predicts spectral types cooler than M9 and that are not covered by our temperature scale. The spectroscopic data provide spectral types with accuracy down to ±0.5 subclass while the spectral types derived from the photometry have been rounded to ±1 subclass.

We adopted throughout this paper the spectral types from the spectroscopic literature, except for the two stars without available spectral types for which we resort to the values derived from $V-J$ as described above. Moreover, we have removed four stars with final spectral classification late K such that the 10-pc sample is reduced to 159 stars.

Figs 2(a) and (b) display the spectral type and the mass distribution of the final 10-pc sample. The masses of all stars were derived from their $T_{\rm eff}$ making use of the 5 Gyr isochrone of the Baraffe et al. (1998) models. The two histograms in Figs 2(a) and (b) are very different reflecting the non-linear transformation between temperature and mass. In the right-hand panel of the figure the mass distribution of the subsamples detected in X-rays, *FUV* and *NUV*, respectively, is displayed. Note that the number of stars with observations and that with detections in one of the three energy bands differs from the numbers given in Sections 2.1.1 and 2.1.2 due to the removal of four K-stars from the sample. In each mass bin the number of detected stars in a given energy band has been normalized to the total number of stars in that mass bin with available data in the same energy band. A detection fraction of 100 per cent is reached only in the *NUV*. For the other two bands, X-rays and *FUV*, the detection fraction ranges between ∼30 and 80 per cent and is remarkably constant as a function of mass. This means that with the presently available instrumentation it is not possible to reach down to the X-ray and *FUV* emission levels of the least active nearby M stars.

The spectroscopic catalogues of Reiners et al. (2012) and Mohanty & Basri (2003) provide, next to the spectral types, information on the rotational velocity ($v \sin i$) and Hα emission. Within the 10-pc sample, 67 stars have an Hα measurement, 25 of them are detections and 42 are upper limits. A measurement for the rotational velocity has been done for 107 stars from the spectroscopic catalogues but for 83 of them this yielded only an upper limit to $v \sin i$.

The relevant stellar parameters of all 159 stars from the 10-pc sample are given in Table 1. Next to the identifiers from LG11 (Column 1) we give in Column 2 the Gl/GJ numbers from the CNS. The subsequent columns represent the distances corresponding to the trigonometric parallaxes given by LG11, the spectral types and effective temperatures as described above and the bolometric flux at Earth, $f_{\rm bol}$. This latter one is obtained from the surface flux, $F_{\rm s,bol} = \sigma_{\rm B} T_{\rm eff}^4$ where $\sigma_{\rm B}$ is the Boltzmann constant, multiplying it with the scaling factor $(\frac{R_*}{d})^2$. The stellar radii (R_*) were derived from Baraffe et al. (1998) models assuming an age of 5 Gyr for all stars. The ±0.5 subclass uncertainties in spectral type correspond to about ±75 K in temperature. According to Baraffe et al. (1998) the stellar radius changes by less than 3 per cent between 1 and 5 Gyr, the likely age of this sample. The errors in the distances are for most stars also very small. Therefore, the uncertainties in $f_{\rm bol}$ are dominated by the uncertainty in the temperature and amount to ≈10 per cent.

2.3 Completeness

To examine the completeness of the 10-pc sample we followed two approaches. First, we compared the sample to the previous samples

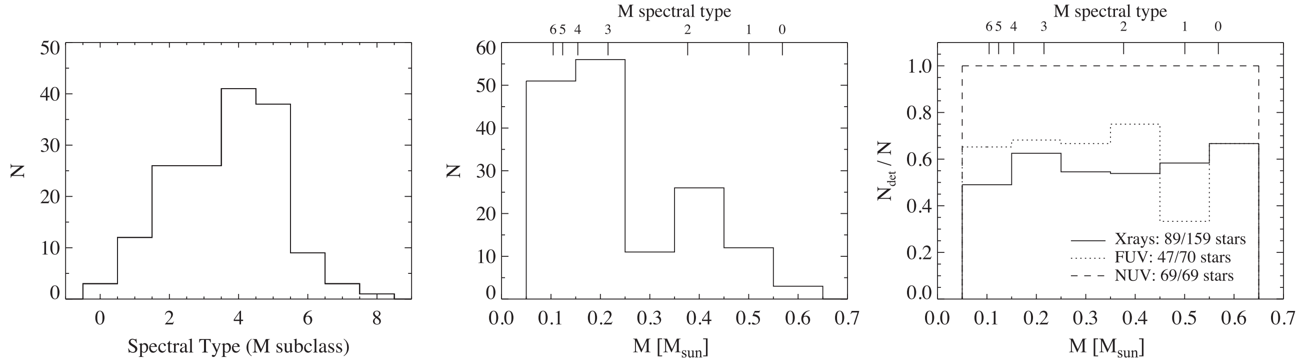

Figure 2. Spectral type (left-hand panel) and mass (middle panel) distribution of the 10 pc-sample. The fractions of the subsample in each mass bin that are detected in X-rays (solid line), *FUV* (dotted line) and *NUV* (dashed line) are shown in the right-hand panel.

Table 1. Stellar parameters for 10-pc M dwarf sample.

Name	Gl/GJ	d (pc)	SpT	$T_{\rm eff}$ (K)	$\log f_{\rm bol,\,Earth}$ (erg cm^{-2} s^{-1})	$v \sin i$ (km s^{-1})
PM I00054−3721	Gl 1	4.34 ± 0.02	M1.5	3575	−7.37	<2.5
PM I00115+5908		9.23 ± 0.12	M5.5	2936	−9.33	…
PM I00154−1608	GJ 1005 AB	4.99 ± 0.25	M4.0	3165	−8.44	<3.0
PM I00184+4401	Gl 15 B	3.56 ± 0.89	M3.5	3241	−8.01	<3.1
PM I01025+7140	Gl 48	8.24 ± 0.08	M3.0	3318	−8.58	<2.5
PM I01026+6220	Gl 49	9.96 ± 0.15	M1.5	3575	−8.10	<3.4
PM I01103−6726	Gl 54	8.20 ± 0.16	M2.0	3500	−8.09	…
PM I01125−1659	Gl 54.1	3.69 ± 0.12	M4.5	3089	−8.30	<2.5

This table is available in its entirety in the electronic edition of MNRAS. Here only the first eight rows are shown to illustrate the format.

of nearby M stars presented in the literature. Secondly, we computed the mass function of the 10-pc sample and compared it to the mass function of field M dwarfs presented by Bochanski et al. (2010).

We noticed that 10 out of 39 stars of the list of M dwarfs within 10 pc studied by Marino, Micela & Peres (2000) are missing in the 10-pc sample. This includes some of the most well-known flare stars, UV Cet, CN Leo and Prox Cen. The absence of one star from the 10-pc sample can be attributed to it being at the border of our distance cut-off [with $d = 11.4$ pc in LG11 but $d < 10$ pc in Marino et al. (2000)]. The remaining nine missing stars imply a completeness of 95 per cent for the 10-pc sample. LG11 consider their full (not distance-limited) M dwarf catalogue ∼90 per cent complete for the Northern hemisphere and ∼60 per cent for the Southern hemisphere. This is qualitatively consistent with the fact that only one of the nine stars missing from the 10-pc sample has positive declination. Assuming that there are no other stars missing in the 10-pc census of LG11 beyond these nine objects, we find a completeness of 99 per cent for the northern and of 89 per cent for the southern sky.

Bochanski et al. (2010) have presented the mass function of low-mass field dwarfs based on SDSS photometry for 15 million stars. In Fig. 3 we reproduce their result for the system mass function (small circles connected by the solid curve). Overplotted is the space density of the 10-pc sample divided into spectral subclasses. Each spectral type bin combines stars with spectral type MX and MX.5, where X = 0, …, 5, and is centred on MX.25. The spectral types were converted to mass with the temperature scale and evolutionary models as described in Section 2.2. We omitted spectral bins at the edge of the samples' mass distribution that are populated by less than 5 stars. In practice, this regards six stars with spectral types M6 and later as the outliers of late-K type have already been removed from the sample. The 10-pc sample is overall in good agreement with the mass function presented by Bochanski et al. (2010) except for the coolest mass bin where a large number of stars seem to be missing. Assuming that we miss half of the stars in the M5 bin, the number necessary to make our sample comply with the mass function of Bochanski et al. (2010) at M5 spectral type, our completeness is $153/(153 + 18)$, i.e. ∼89 per cent. The 'missing stars' from Marino et al. (2000), indeed, have a peak in this bin (see open squares in Fig. 3).

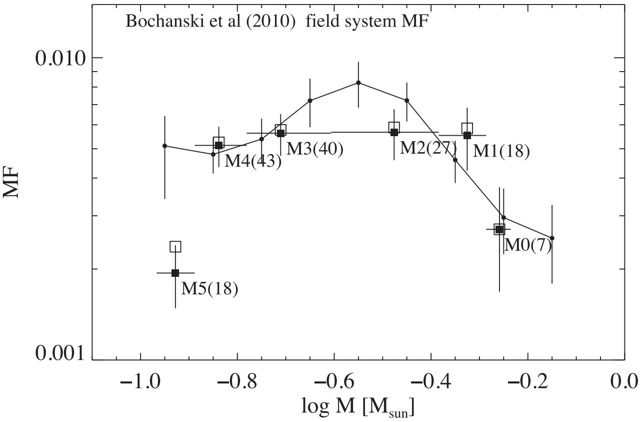

Figure 3. Space density of the 10-pc sample (filled squares) compared to the M dwarf mass function from Bochanski et al. (2010) (shown as small circles connected by a solid line). Numbers in brackets indicate the number of stars in each spectral type bin for the 10-pc sample. Open squares represent the 10-pc sample incremented by the nine missing stars from Marino et al. (2000).

3 ACTIVITY DIAGNOSTICS

3.1 X-ray fluxes

First, the X-ray data compiled from the various catalogues that we have cross-correlated with the 10-pc sample must be brought into a homogeneous shape. The RASS catalogues and the 2RXP list count rates in the *ROSAT*/PSPC energy band and the 2XMMi-DR3 catalogue gives fluxes in various energy bands between 0.2 and 12 keV. These fluxes refer to a power-law spectrum with index $\Gamma = 1.7$ absorbed by $N_{\rm H} = 3 \times 10^{20}$ cm^{-2} (Watson et al. 2009). We have extracted the 0.2–2.0 keV fluxes assuming a thermal one-temperature spectrum from all X-ray data described in Section 2.1.1 as follows.

Concerning the 2XMMi-DR3 data, we must note that a power law is representative for X-ray emission generated by non-thermal electrons and is not adequate for describing the thermal coronal X-ray emission. Moreover, the interstellar absorption of nearby stars is much smaller than assumed in the 2XMMi-DR3. We calculated the count-to-flux conversion factors (CFs) for a thermal one-temperature model (APEC) of $kT = 0.3$ keV[2] and a column density of 10^{19} cm^{-2}, corresponding to the average interstellar extinction at 10 pc. The fluxes in the 2XMMi-DR3 energy bands were then corrected using the ratio between the (power-law) CFs used in the

---

[2] Our estimate of the coronal temperature is based on previous X-ray studies of late-type stars, e.g. for solar analogues there is an empirical power-law relation between X-ray luminosity and temperature with $T \sim 2 - 6$ MK for $\log L_{\rm x}$ [erg s^{-1}] = 27, …, 29 (Güdel 2004). This corresponds approximately to the range of X-ray luminosities of the 10-pc sample.

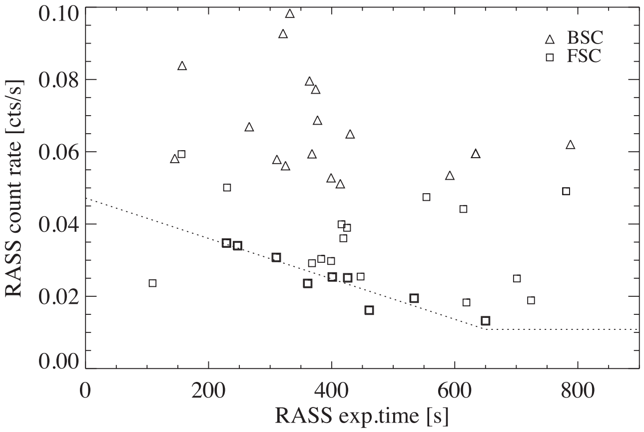

Figure 4. Count rate for stars from the 10-pc sample from the RASS BSC (triangles) and FSC (squares) as a function of the exposure time. The dotted line is the empirical lower envelope that defines the sensitivity limit. The linear part was determined by fitting the stars represented by thicker plotting symbols. For exposure times larger than 650 s, we assumed a constant upper limit count rate.

XMM–Newton Serendipitous Source Catalog[3] and the APEC CFs calculated by us. Finally, we summed up the corrected 2XMMi-DR3 fluxes from the three lowest energy bands to obtain the 0.2–2.0 keV flux. (For better comparison with *ROSAT* fluxes we do not consider the higher *XMM–Newton* energy bands from 2.0 to 4.5 keV and from 4.5 to 12 keV.) The PSPC count rates from the *ROSAT* catalogues are translated into 0.2–2.0 keV fluxes using the same thermal model as for the *XMM–Newton* data ($CF_{\rm ROSAT} = 2.03 \times 10^{11}$ cts erg^{-1} cm^{-2}).

About 40 per cent of the stars in the 10-pc sample have no X-ray detection, and we calculated their upper limits after having extracted the sensitivity limit making use of the RASS detections as follows. Fig. 4 shows those stars from the 10-pc sample that were detected in the RASS BSC or FSC. The lower envelope of the distribution of count rate versus exposure time defines the RASS sensitivity threshold. We obtained a numerical value for the count rate upper limit as a function of the RASS exposure time by performing a linear fit to the lowest observed count rates for given exposure time (dotted line in Fig. 4). For large exposure times a constant sensitivity limit is assumed. This is a conservative assumption considering that for long observations the sensitivity becomes background limited and decreases as the square root of the exposure time. We extracted the RASS exposure time for the proper-motion-corrected ICRS position of each of the undetected stars from the HEASARC archive,[4] and placed them on the sensitivity curve to obtain their upper limit count rate. Then $CF_{\rm ROSAT}$ was applied for the conversion to the 0.2–2.0 keV flux.

There are 25 stars in the 10-pc sample that are reported in more than one of the X-ray catalogues that we have searched, allowing us to look for evidence of variability. For those stars, the X-ray flux from the pointed observations is compared to the X-ray flux from the RASS in Fig. 5. The majority of stars do not display variations larger than about a factor of 2. This is consistent with an earlier variability study of M dwarfs by Marino et al. (2000).

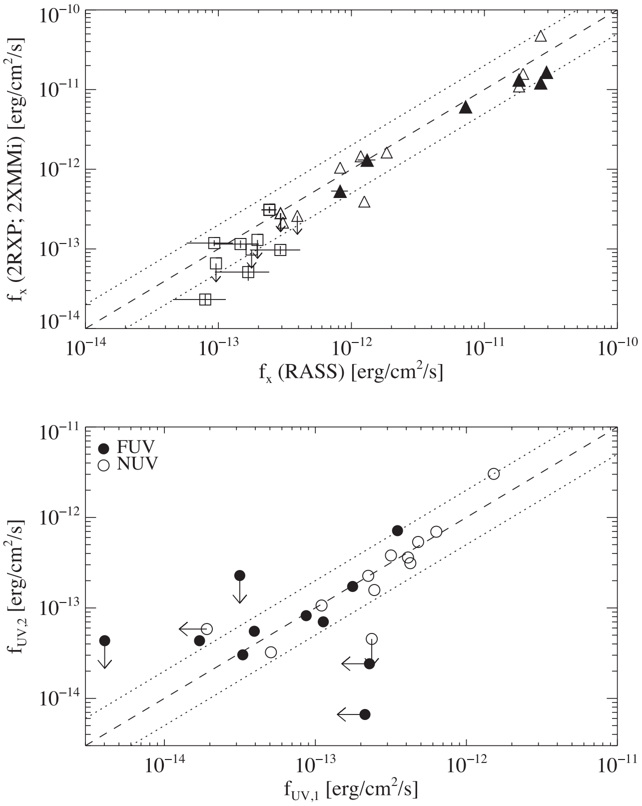

Figure 5. Comparison of X-ray and UV flux from multiple observations of a given star. Top: pointed X-ray data versus RASS for the stars with multiple X-ray detections; bottom: both *FUV* (filled circles) and *NUV* (open circles).

Having verified the negligible role of variability, we can consider a single measurement for each star to be representative for its X-ray emission level. We selected the flux from the 2RXP if available else the flux from the BSC or the FSC. Only if no *ROSAT* detection is available we resort to the 2XMMi. For the undetected stars we use the RASS upper limits.

The X-ray fluxes and upper limits of all stars from the 10-pc sample are listed in Table 2 together with their uncertainties in squared brackets. For further analysis, the X-ray fluxes and their upper limits were transformed into luminosities and their upper limits using the individual distances listed in Table 1.

3.2 UV fluxes

FUV and *NUV* magnitudes in the AB-system within a 12.8 arcsec diameter of the source position were extracted for all detections in the 10-pc sample. This diameter is a good compromise between the large apertures required to gather almost all of the *GALEX* flux and the small ones that are optimal for minimizing the background. Flux densities were computed from the *FUV* and *NUV* magnitudes using the transformation relations given by Bianchi (2009), and they were converted to fluxes with the effective band width[5] of the respective *GALEX* filter ($\delta\lambda_{FUV} = 268$ Å; $\delta\lambda_{NUV} = 732$ Å).

The upper limits of the stars that are undetected in the *FUV* band were estimated as follows. We obtained the *FUV* upper limit of PM I03133+0446S (GJ 1057), the only star undetected in the MIS,

---

[3] The count-to-flux CFs used in the *XMM–Newton* Serendipitous Source Catalog are available at http://xmmssc-www.star.le.ac.uk/Catalogue/2XMM/UserGuide_xmmcat.html#Tab ECFs.

[4] http://heasarc.gsfc.nasa.gov/cgi-bin/W3Browse/w3browse.pl

[5] See *GALEX* Observer's guide available at http://galexgi.gsfc.nasa.gov/docs/galex/Documents/ERO_data_description_2.htm

Table 2. Observed *NUV*, *FUV* and X-ray fluxes for 10-pc sample. Flux units are erg $\mathrm{cm^{-2}\,s^{-1}}$. Lower and upper values for the fluxes derived from the uncertainties are given in brackets.

Name	$\log f_{NUV}$	$\log f_{NUV,\mathrm{lo}}, f_{NUV,\mathrm{up}}$		$\log f_{FUV}$	$\log f_{FUV,\mathrm{lo}}, f_{FUV,\mathrm{up}}$		$\log f_{\mathrm{X}}$	$\log f_{\mathrm{X,\,lo}}, f_{\mathrm{X,\,up}}$
PM I00054−3721	−13.14	[−13.10, −13.17]	<	−13.76			−13.01	[−12.96, −13.07]
PM I00115+5908						<	−13.20	
PM I00154−1608	−14.15	[−13.93, −14.37]	<	−13.71			−13.41	[−13.29, −13.58]
PM I00184+4401							−11.89	[−11.85, −11.94]
PM I01025+7140	−12.97	[−12.93, −13.02]		−13.22	[−12.95, −13.48]		−13.19	[−13.03, −13.43]
PM I01026+6220						<	−13.27	
PM I01103−6726	−12.97	[−12.93, −13.01]		−13.21	[−13.00, −13.43]	<	−12.87	
PM I01125−1659	−13.10	[−13.05, −13.14]		−12.70	[−12.60, −12.80]		−12.41	[−12.36, −12.45]

This table is available in its entirety in the electronic edition of MNRAS. Here only the first eight rows are shown to illustrate the format.

using the background-subtracted *GALEX*/*FUV* intensity image. We computed the *FUV* magnitude of PM I03133+0446S within a circular aperture centred on the star and with the same diameter as the aperture used for the detected sources. All remaining undetected stars were observed in the AIS. We estimated the *FUV* upper limits for five of them, spanning all the range of exposure times, in the same manner as for PM I03133+0446S. The upper limits of the others were then obtained by linear interpolation between these values.

There are 12 stars with two *NUV* observations and 11 stars with two *FUV* observations. These objects can be investigated for UV variability analogous to the case of the X-ray emission in Section 3.1. The bottom panel of Fig. 5 compares the fluxes for stars with two measurements in the *FUV* and/or the *NUV* band. Overall, there is little evidence for variability. Only the upper limits are far off from the 1:1 relation. However, all *FUV* upper limits are compatible with the detections, and they are shallow due to the low exposure time in the respective observation. The only star that has shown strong variability is PM I09307+0019 (GJ 1125). Its *NUV* upper limit is more sensitive than its *NUV* detection. This is not a contradiction because the exposure times of its two observations were different by about a factor of 10. In the remainder of this paper, we used for stars that are detected in two observations of a given *GALEX* band, the average of the two measurements. Observed but undetected stars are represented by their upper limits. We ignore the upper limits of stars that also have a detection in another *GALEX* observation.

Analogous to the X-ray fluxes, we list the *FUV* and *NUV* fluxes in Table 2. Luminosities in the two *GALEX* bands were calculated from the fluxes in the same way as for the X-ray band (see Section 3.1).

3.3 Hα fluxes

The spectroscopic catalogues described in Section 2.2 give the Hα to bolometric flux ratio ($\log(f_{\mathrm{H}\alpha}/f_{\mathrm{bol}})$) that we designate 'activity index' in Section 3.4. We have extracted the observed fluxes from this quantity reversing the approach for obtaining the UV activity index described next.

3.4 Activity indices

In analogy to the standard measure for Ca II H+K activity, we define the UV activity index as

$$R'_{\mathrm{UV}} = \frac{f_{\mathrm{UV,exc}}}{f_{\mathrm{bol}}} = \frac{f_{\mathrm{UV,obs}} - f_{\mathrm{UV,ph}}}{f_{\mathrm{bol}}}, \tag{1}$$

where $f_{\mathrm{UV,\,exc}}$ is the UV excess flux attributed to activity, i.e. the difference between the observed UV flux ($f_{\mathrm{UV,\,obs}}$) and the photospheric flux in the same UV band ($f_{\mathrm{UV,\,ph}}$), and f_{bol} is the bolometric flux. The bolometric flux is obtained from the surface flux as described in Section 2.2.

In equation (1) 'UV' stands for the *NUV* and *FUV* bands, respectively. The superscript ($'$) indicates that the ratio has been corrected for photospheric emission. The photospheric contribution to the *NUV* and *FUV* emission was estimated with the help of the synthetic DUSTY spectra of Allard et al. (2001). We adopted for each star in the 10-pc sample the model spectrum with solar metallicity, $\log g = 5$ and with T_{eff} corresponding to the spectral type from the references described in Section 2.2. Fig. 6 shows two examples of observed SEDs and corresponding DUSTY model. The synthetic spectra are available in terms of surface flux density and have been transformed for this plot into observed flux density by applying the dilution factor $(\frac{R_*}{d})^2$. As before in Section 2.2 we have used for the stellar radius the value extracted from the 5 Gyr isochrone of Baraffe et al. (1998) for the known effective temperature of each star. As mentioned in Section 2.2, no significant difference in radius is predicted for ages between 1 and 5 Gyr.

For many stars, when comparing the observed flux densities to the model spectra as described above we noticed serious problems with the normalization. If the distance is assumed to be known from the trigonometric parallax for each star, for those cases an unrealistically large radius was needed to make the model spectrum fit the observed photometry. A larger radius corresponds for given T_{eff} to a smaller gravity, i.e. a younger age. We come back to this problem in the next paragraph. First, we describe how the photospheric UV fluxes have been derived. We can avoid directly dealing with the uncertain radius by computing the photospheric UV flux density from the $UV - J$ colour predicted from the DUSTY model and the observed J-band flux density ($(f_{\mathrm{J}})_\lambda$),

$$(f_{\mathrm{UV,ph}})_\lambda = \frac{(F_{\mathrm{UV,DUSTY}})_\lambda}{(F_{\mathrm{J,DUSTY}})_\lambda} \cdot (f_{\mathrm{J}})_\lambda. \tag{2}$$

The theoretical UV and J-band flux densities, $(F_{\mathrm{UV,\,DUSTY}})_\lambda$ and $(F_{\mathrm{J,\,DUSTY}})_\lambda$, were obtained by convolving the synthetic spectrum with the respective normalized filter transmission curve as described by Bayo et al. (2008). The photospheric UV flux densities from equation (2) were converted to fluxes ($f_{\mathrm{UV,\,ph}}$) in the same manner as the observed flux densities by multiplying with the effective filter band width (see Section 3.2).

To test the effect of $\log g$ and radius on the photospheric UV emission we have repeated the evaluation of equation (2) for DUSTY models of $\log g = 4.5$. This gravity corresponds to an age of $\log t\,[\mathrm{Myr}] = 7.5$ according to Baraffe et al. (1998). We find that the photospheric

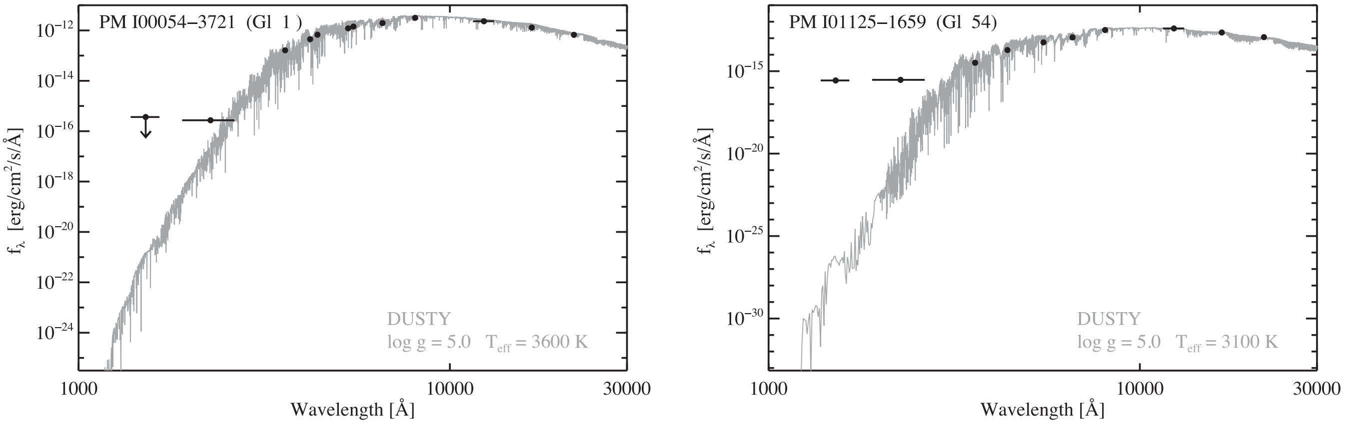

Figure 6. Examples of observed SEDs for two stars from the 10-pc sample compared to the DUSTY model spectrum selected as described in Section 3.4. The photometry was compiled from data archives and catalogues: *Tycho-2* and *Hipparcos* (Høg et al. 2000; Perryman & ESA 1997), SDSS DR7 (Adelman-McCarthy et al. 2009), 2MASS (Cutri et al. 2003) and multi-band photometry from Koen et al. (2010). The two left-most data points represent the *GALEX FUV* and *NUV* bands.

UV flux is smaller and the UV excess larger by up to a factor of 2 with respect to our assumption of $\log g = 5$. However, the age related to this low gravity would imply a pre-main-sequence status for a large fraction of the 10-pc sample. An investigation of the age of individual stars on the basis of a comparison to model predictions is not the scope of this paper. Therefore, we use throughout the remainder of this paper the UV fluxes and chromospheric excess fluxes derived for $\log g = 5.0$ but keep in mind that they may be up to a factor of 2 higher in individual cases.

Similarly to the UV, the ratio of X-ray flux to bolometric flux is defined as $R_{\rm X}$. Here no photospheric flux is considered because the photosphere is not expected to produce emission in the X-ray band.

For the Hα emission we resort directly to the values computed by Reiners et al. (2012) and Mohanty & Basri (2003).

4 CHARACTERISTICS OF ACTIVITY ON M DWARFS

In the following we examine the connection between various activity diagnostics and their relation with other stellar parameters such as effective temperature and rotation rate. For the UV which is poorly explored so far we provide a comparison to available literature data. Unless stated otherwise, all our UV measurements refer to the chromospheric excess flux after subtraction of the photospheric contribution as described in Section 3.4.

4.1 Chromospheric versus photospheric UV flux

The chromospheric emission resulting in excess flux with respect to the photospheric model is shown in Fig. 7 for the *NUV* band. Here, the excess is normalized to the observed *NUV* flux. The lower envelope of these data represents the maximum observed contribution of the photosphere to the *NUV* emission for a given $T_{\rm eff}$. For the majority of stars the dominating contribution to the *NUV* emission comes from the chromosphere. In fact, no star has purely photospheric *NUV* emission. However, for several stars the photosphere contributes ∼20–30 per cent to the *NUV* emission, and for the most extreme cases the photosphere produces more than half of the observed *NUV* flux. The higher the effective temperature the larger on average the contribution of the photosphere to the *NUV* emission. This is not surprising considering that the SED shifts towards the blue for hotter stars. The fact that the data points are distributed below the horizontal line representing 100 per cent chromospheric *NUV* flux in Fig. 7 shows that subtracting the photospheric part of the *NUV* emission is essential for a correct assessment of the chromospheric emission.

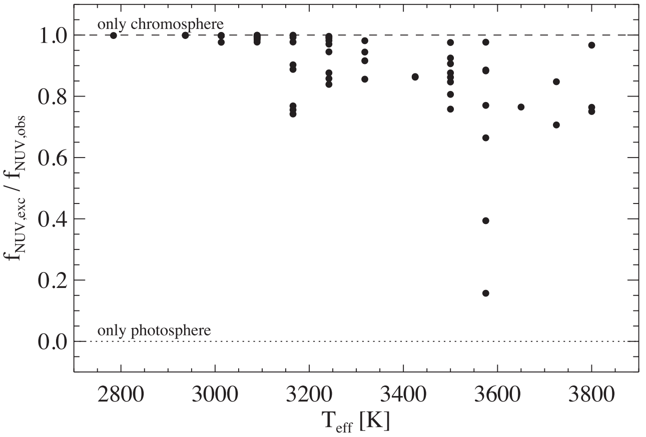

Figure 7. Fraction of *NUV* emission in excess of the photospheric model spectrum. Horizontal lines define stars for which all *NUV* emission is from the chromosphere (dashed) or from the photosphere (dotted).

An analogous analysis in the *FUV* has shown that in this energy band all photospheres in our sample are very faint, such that the chromospheric excess amounts to ≥99 per cent of the observed emission.

4.2 High-energy spectral energy distributions

The ‘SED’ of the excess emission can be studied by means of a UV colour representing the excess emission and defined as

$$FUV_{\rm exc} - NUV_{\rm exc} = -2.5 \log \left(\frac{f_{\rm exc}, FUV}{f_{\rm exc}, NUV} \right) \quad (3)$$

where $f_{{\rm exc},\,FUV}$ and $f_{{\rm exc},\,NUV}$ are the chromospheric excess fluxes defined in Section 3.4. In Fig. 8, we show this colour in dependence of the X-ray surface flux as a measure of the activity level. Only stars detected in all three energy bands (X-rays, *FUV* and *NUV*) are shown. For highly (X-ray) active stars the *FUV* excess dominates the *NUV* excess, while for weaker X-ray emitters the *NUV* excess is stronger than the *FUV* excess.

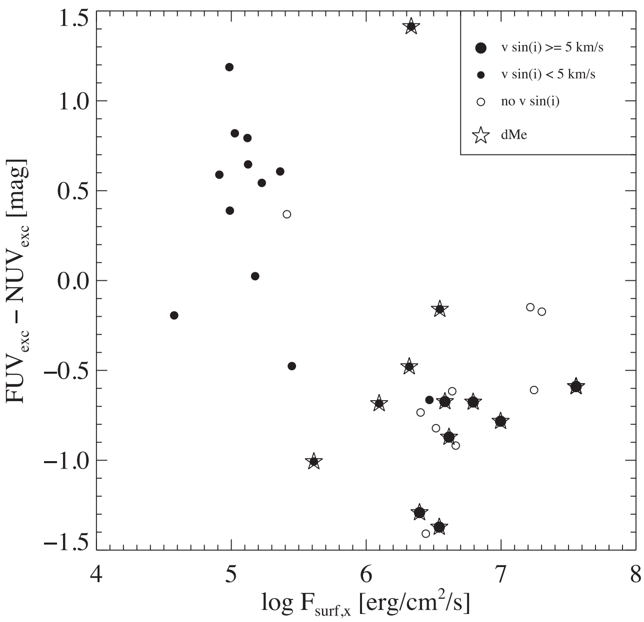

Figure 8. 'Colour' representing *FUV* versus *NUV* excess in function of X-ray surface flux. Hα emitting stars (dMe) are highlighted. Fast and slow rotators and stars without information on $v \sin i$ are distinguished by different plotting symbols.

4.3 Relations between Hα, UV and X-ray emission

Various chromospheric lines have been shown for different samples of late-type main-sequence stars to be connected by a power-law relation of the type

$$\log F_1 = c_1 + c_2 \log F_2, \tag{4}$$

where $F_{1,2}$ are the surface fluxes representing two different activity diagnostics and c_1 and c_2 are coefficients. Early comparisons of coronal X-ray and chromospheric emission line fluxes in samples of late-type dwarfs have suggested a spectral type dependence of the slopes (e.g. Schrijver & Rutten 1987; Doyle 1989). However, Martínez-Arnáiz et al. (2011) found on a much larger sample that the flux–flux relations are universal in spectral type but with a separate branch for the most active stars. Stelzer et al. (2012) have for the first time extended these relations into the regime of the ultracool (late-M) dwarfs.

Here, we search for flux–flux relations in the broad-band UV and X-ray emission together with Hα emission for the 10-pc sample. The surface fluxes in all activity diagnostics were calculated using the individual radii determined as described in Section 3.4. The results are shown in Fig. 9 where the size of the plotting symbols is used to distinguish fast from slow rotators and different colour codes are used for detections and upper limits.

Considering only the detections, the pair of activity diagnostics with the smallest spread is *NUV* versus *FUV*. We have performed linear regression fits to different pairs of fluxes considering only the stars detected in both involved energy bands. As in our previous works, the method used is the least-squares bisector regression described by Isobe et al. (1990). The results are overplotted in Fig. 9 and the coefficients of the log–log relations are given in Table 3. We have omitted one star (Gl 169.1 A) from the fit of *NUV* versus X-ray emission. Its very high *NUV* flux places it orders of magnitude above the bulk of the stars and may be due to a flare event. Note also that the inclusion of the upper limits might modify the relations.

Another representation of the flux–flux relationships is shown in Fig. 10. Here, for the comparison of X-ray and UV fluxes we consider separately Hα emitters (dMe stars) and stars with upper limit to the Hα flux (dM stars). Fig. 10 shows that the dM stars are generally located on the extension of the flux–flux relation for dMe stars.

Relations between luminosities or activity indices of two spectral bands can be examined analogous to the case of the flux–flux relationships. The results are summarized in Table 3.

4.4 Activity indices versus spectral type and rotation rate

The distribution of the activity indices for all four diagnostics (Hα, X-rays, *FUV* and *NUV*) is shown in Fig. 11 as a function of $T_{\rm eff}$ and $v \sin i$. Upper limits are symbolized by grey downward pointing arrows. The Hα sample is restricted in spectral type by the available published spectroscopic data. For conclusions on the Hα activity of early-M dwarfs we refer to Reiners et al. (2012) who have studied a much larger sample. We used the Hα data here as comparison to our new data for the X-ray, *FUV* and *NUV* emission of the 10-pc sample.

For the X-ray band, the lower envelope of the activity index increases with decreasing effective temperature. The location of the upper limits suggests that this is related to the reduced sensitivity in $R_{\rm X}$ for the cooler stars which are fainter in terms of bolometric flux. There is no obvious slope of the lower envelope for the *FUV* and the *NUV*.

A spread of several orders of magnitude is observed in all activity indices for a given $T_{\rm eff}$. This spread corresponds to a range of rotational velocities. In fact, the spread in the activity indices is largest at spectral type around M4 where the largest range of $v \sin i$ is observed. For each spectral subclass, fast rotators show higher activity levels than slow rotators in agreement with the common rotation/activity paradigm.

There seems to be a transition in the rotation rates between early-M ($\leq$ M3) and mid- to late-M ($\geq$ M4) (see also Reiners et al. 2012). All early-M dwarfs in the 10-pc sample have very low or undetectable rotation rate. On the contrary, fast rotation is observed in about half of the stars with spectral type M4 and later. In terms of $R_{\rm H\alpha}$, and less pronounced in $R_{\rm x}$, the fast rotators form a plateau in the right-hand panels of Fig. 11, i.e. the level of activity does not depend on rotation. This 'saturation' is ubiquitously observed in the activity indices of late-type stars, yet there is no consensus on its origin. Vilhu (1984) attributed it to a complete coverage of the stellar surface with active regions. Alternative explanations are saturation of the power of the dynamo (Vilhu & Walter 1987), a redistribution of the radiative losses between emission lines and continuum (Doyle 1996) and changes of magnetic field structure (Jardine & Unruh 1999).

The evidence for saturation in R'_{NUV} and R'_{FUV} is less clear than for $R_{\rm H\alpha}$ and $R_{\rm X}$. We can determine the mean level of each activity index in the presumed saturated regime. For this analysis we restricted the sample to stars with $v \sin i \geq 5\,{\rm km\,s^{-1}}$. Beyond this value H$\alpha$ and X-ray activity indices have reached a plateau in the right-hand panel of Fig. 11. The average activity indices and its standard deviation for this subsample of fast rotators are given in Table 4. The trend for the broad-bands (*NUV*, *FUV*, X-rays) goes for increasing mean activity level with increasing atmospheric height. However, the small number of stars evaluated leads to a rather large spread. The Hα emission which is produced in the chromosphere, i.e. relatively low in the atmosphere, is in agreement with this trend as it presents the faintest saturation level.

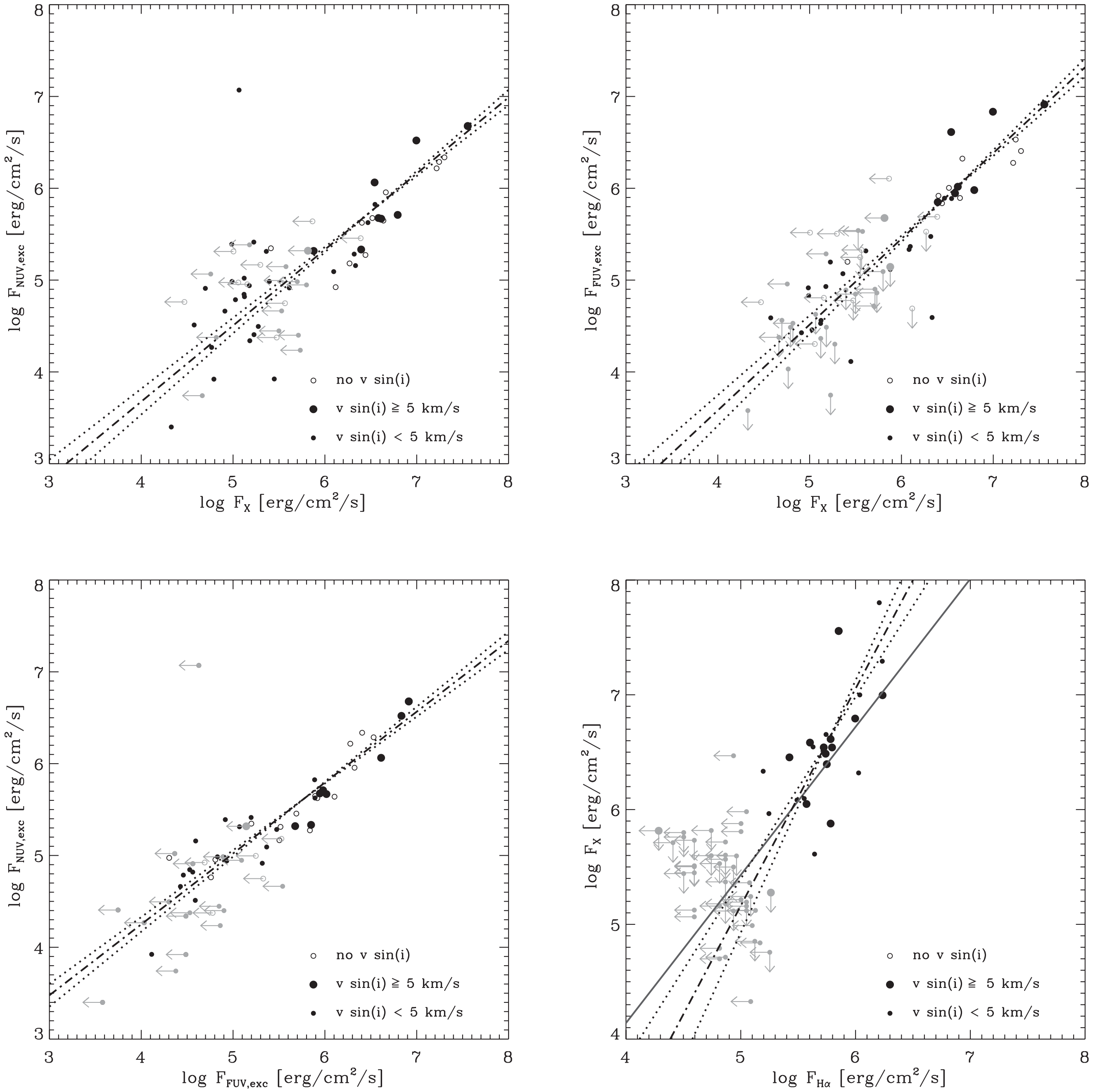

Figure 9. Flux–flux relationships for UV, X-ray and Hα emission. The size of the plotting symbols characterizes the rotation rates. Upper limits are drawn as grey arrows. Linear regression fits to the detections (black symbols) are shown as dash–dotted lines and their variance as dotted lines. The flux–flux relation derived by Stelzer et al. (2012) for a sample of M dwarfs including ultracool dwarfs is overplotted as solid line in the bottom-right panel.

Slow rotators ($v \sin i \leq 3\,\mathrm{km\,s^{-1}}$) cover a large range of observed activity levels. Whether activity depends on rotation in that regime is difficult to determine because the available sensitivity limits in terms of the rotation rate are too high and because the rotation rate is only a lower limit due to the unknown inclination angle.

4.5 Comparison with published UV data of M dwarfs

We have searched the literature for spectroscopic data in the UV that would allow us to evaluate the relative contributions of lines and continuum to the *GALEX* fluxes. While detailed UV spectroscopy has been presented for a few individual M dwarfs (e.g. Pagano et al. 2000; Hawley et al. 2003, 2007), published chromospheric line fluxes are found for very few stars of the 10-pc sample. Among the most notable and best-studied emission features in dwarf stars are the chromospheric Mg II h+k doublet at $\lambda\lambda$2796, 2803 Å in the *NUV* and the C IV$\lambda\lambda$1548, 1550 Å doublet from the transition region in the *FUV*. Mathioudakis & Doyle (1989, henceforth MD89) have listed Mg II surface fluxes ($F_{\mathrm{s,Mg\,II}}$) for K-M dwarf stars based on *IUE* spectra. Their sample has 18 stars in common with ours. Further fluxes for *FUV* and *NUV* continuum as well as some important UV emission lines from M dwarfs are presented by France et al. (2013,

Table 3. Coefficients of double-logarithmic relations of the type shown in equation (4) for three different measures for activity (surface flux, activity index and luminosity) and four energy bands (Hα, *NUV*, *FUV* and X-rays).

Line 1	Line 2	N_*	c_1	c_2
		Surface flux		
X	Hα	24	-4.29 ± 1.77	1.89 ± 0.31
FUV	X	36	-0.16 ± 0.43	0.93 ± 0.07
NUV	X	46	0.36 ± 0.36	0.83 ± 0.06
NUV	*FUV*	46	1.16 ± 0.26	0.77 ± 0.04
		Activity index		
X	Hα	24	4.43 ± 1.23	1.90 ± 0.31
FUV	X	36	-0.79 ± 0.21	0.94 ± 0.06
NUV	X	46	-1.39 ± 0.19	0.81 ± 0.05
NUV	*FUV*	46	-1.13 ± 0.16	0.76 ± 0.04
		Luminosity		
X	Hα	24	-15.71 ± 6.27	1.61 ± 0.23
FUV	X	36	1.11 ± 2.26	0.94 ± 0.08
NUV	X	46	0.92 ± 1.70	0.94 ± 0.06
NUV	*FUV*	46	2.58 ± 1.34	0.90 ± 0.05

henceforth FFL13) in their study of *HST* Cosmic Origins Spectrograph (COS) and STIS spectra of six exoplanet host stars. Two of their stars are in common with the 10-pc sample. The UV emission of one of them, GJ 876, has been examined in detail in another dedicated study by France et al. (2012). In the following we compare the fluxes given in those works to our *GALEX* measurements.

As we aimed at a homogeneous data analysis we could not simply compare the surface line fluxes given by MD89 to the *GALEX* fluxes but had to reconvert them to observed fluxes ($f_{\mathrm{obs,Mg\,II}}$) following the inverse of the procedure that was applied by MD89. These authors have computed the ratio $F_{\mathrm{s,Mg\,II}}/f_{\mathrm{obs,Mg\,II}}$ using a relation that involves the *V*-band magnitude, the $R - I$ colour, the effective temperature and a bolometric correction (*B.C.*) [see Oranje, Zwaan & Middelkoop (1982) for details]. They did not list the photometry they used. To be as close as possible to their historic measurements we have compiled *VRI* magnitudes from CNS 3 catalogue. Again for reasons of consistency with MD89, we extracted T_{eff} and *B.C.* from Johnson (1966). The observed Mg II fluxes recovered this way were then transformed back into surface fluxes using the distances from LG11 and the stellar radii derived in Section 3.4. The observed fluxes listed by FFL13 were transformed into surface fluxes in the same way.

We plot the flux–flux relations for the *GALEX/NUV* band and various *NUV* measurements from the literature in Fig. 12. Filled plotting symbols are for Mg II line fluxes and open symbols for broad-band *NUV* fluxes from *HST* STIS. Objects with Mg II line fluxes from MD89 and from FFL13 are shown with different plotting symbols. Several literature measurements for a given star are connected by a vertical line. To make the *GALEX* fluxes comparable to the literature values we plotted here the observed fluxes that include also the photospheric contribution. Fig. 12 shows that the two available total *NUV* fluxes from *HST* STIS are nearly a factor of 10 higher than those from *GALEX*. The Mg II fluxes are on average roughly a factor of 2 lower than the *GALEX/NUV* fluxes.

Analogous to the investigation of the *NUV* line and broad-band emission, we have compared the *GALEX/FUV* to the C IV and to the broad-band *FUV* emission from *HST* COS for the two stars from the 10-pc sample with data in FFL13. We find that the two stars behave very differently. Similar to the *NUV*, for Gl 876 the *HST/FUV* flux is much larger than the *GALEX/FUV* flux ($F_{FUV,\,HST}/F_{FUV,\,GALEX} \approx 6.5$) while the C IV line flux is similar to the *GALEX/FUV* flux ($F_{\mathrm{C\,IV}}/F_{FUV,GALEX} \approx 0.8$). On the contrary, for Gl 832 the broad-band fluxes of the two instruments are within a factor of 2 ($F_{FUV,\,HST}/F_{FUV,\,GALEX} \approx 0.5$) and the C IV flux is much smaller than the *GALEX/FUV* flux ($F_{\mathrm{C\,IV}}/F_{FUV,\,GALEX} \approx 0.04$).

The comparison of the broad-band fluxes must take into account the different wavelength ranges of the instruments. In the case of the *NUV* this is 2300–3050 Å for STIS and 1771–2831 Å for the *GALEX* filter. In particular, we recall that the bulk of Mg II is not being captured by the *GALEX NUV* band which has very low transmission near the cut-off of the filter. However, Mg II makes only about 10 per cent of the total STIS *NUV* emission. Therefore, the differences in the *NUV* broad-band fluxes of the two instruments are likely due to variability. Similarly, variability may be responsible for the differences between the *FUV* fluxes observed with *GALEX* and with the two *HST* instruments. In fact, both stars from FFL13 showed evidence of *FUV* flaring activity during the *HST* observations while no information is given by FFL13 on the *NUV* variability. We note that the *HST* STIS and COS observations of a given star are not simultaneous. The overall impact of the flares on to the *FUV* emission of the stars could not be quantified because no light curves are presented by France et al. (2012) and FFL13 for C IV or for the broad-band emission.

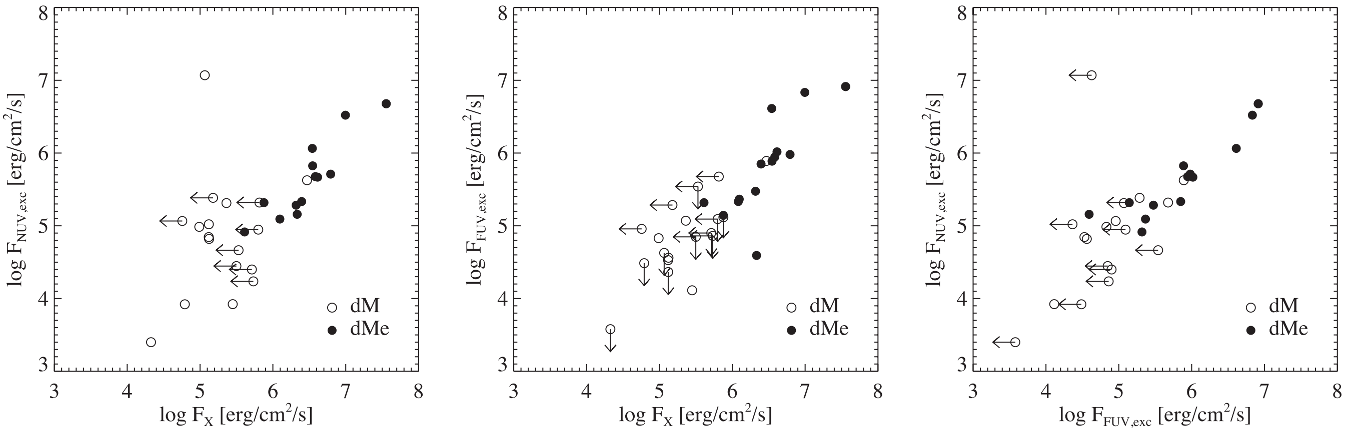

Figure 10. Flux–flux relationships for UV versus X-ray emission distinguishing Hα emitting dMe stars from those without detected Hα emission (dM stars).

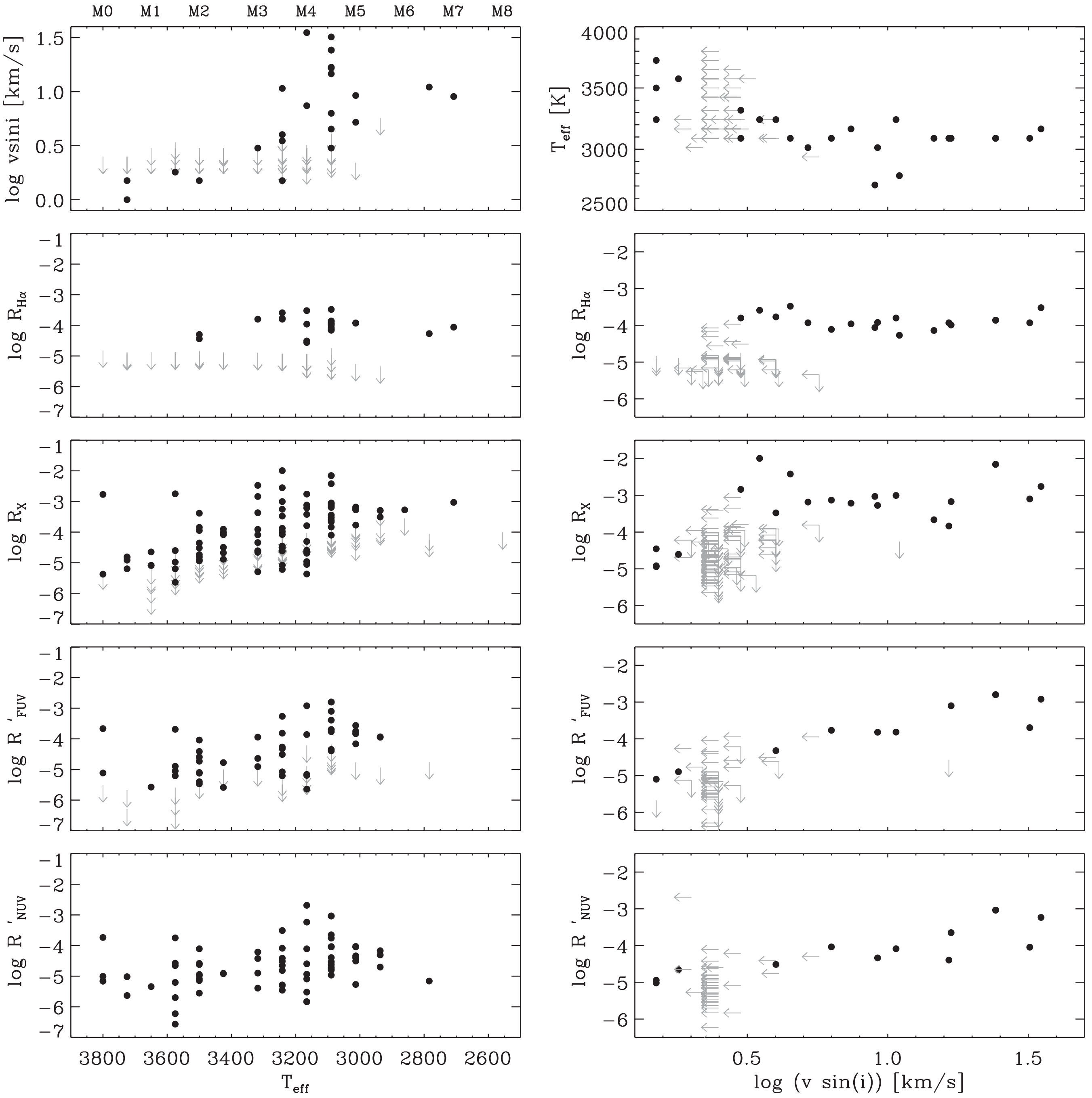

Figure 11. Activity indices in the X-ray, *FUV* and *NUV* bands and Hα emission versus effective temperature (left) and versus rotational velocity (right). Upper limits are represented by grey arrows. For the *FUV* and *NUV* only the excess emission over the photosphere is taken into account. The topmost panels show as a reference log $v \sin i$ (left) and $T_{\rm eff}$ (right), respectively.

4.6 Age evolution

With the aim to study the age evolution of the activity of M dwarfs we have compiled a catalogue of all known M-type members of the TW Hya association (TWA). The TWA represents an excellent comparison sample of pre-main-sequence M dwarfs because at its age of 10 Myr most association members have terminated the accretion process such that the Hα, UV and X-ray emission can be clearly ascribed to magnetic activity.

4.6.1 TWA sample and analysis

Our TWA catalogue comprises all stars considered to be association members by Mamajek (2005) and three further members discovered since by Looper et al. (2007, 2010a,b) and Shkolnik et al. (2011). The X-ray and UV data were extracted in the same way as those of the field M dwarfs (see Sections 2.1.1 and 2.1.2), except that we have consulted only the RASS BSC and FSC catalogues and no X-ray catalogue of pointed observations.

Table 4. Average emission level in the activity indices for fast rotating M dwarfs ($v \sin i \geq 5\,\mathrm{km\,s^{-1}}$), standard deviation and number of stars.

Act. index	Mean	Std. dev	N_*
$\log R_{\mathrm{X}}$	−3.18	0.57	15
$\log R'_{FUV}$	−3.52	0.58	10
$\log R'_{NUV}$	−3.82	0.54	10
$\log R_{\mathrm{H\alpha}}$	−4.04	0.40	15

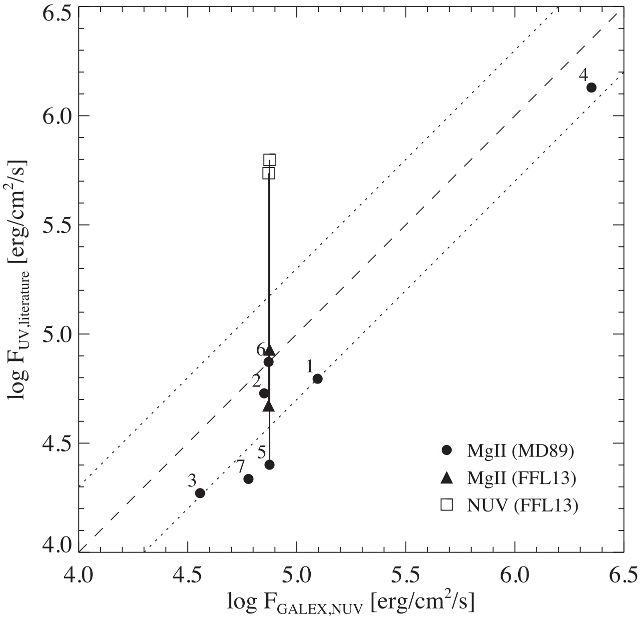

Figure 12. Flux–flux relation for *NUV* measurements from the literature and *GALEX*/*NUV* broad-band. The literature data comprise Mg IIλ 2800 Å line emission published by MD89 (circles) and by FFL13 (triangles) and broad-band emission in 1150–1790 Å excluding Lyα (FFL13). The Mg IIλ 2800 Å data points from MD89 are labelled with numbers corresponding to the following stars: 1 – Gl 83.1, 2 – Gl 411, 3 – Gl 412 A, 4 – Gl 803, 5 – Gl 832, 6 – Gl 876, 7 – Gl 908. Two of them (Gl 832 and Gl 876) have data from FFL13. All literature data for these two stars are connected with a vertical line. The dashed line denotes the 1:1 relation and the dotted lines represent a factor of 2 difference between the two measurements.

A significant fraction of TWA members are close binaries that are not resolved in the RASS and with *GALEX*. For these cases we have distributed the observed X-ray and UV flux equally on both components, unless for TWA11 where the primary is an A-type star and the X-ray emission is likely produced by the secondary M-type component. Limiting the sample to M spectral types and treating the binaries as described, the TWA sample comprises 23 objects. 16 of these are identified with a RASS/BSC source and one with a RASS/FSC source, while 10 are detected with *GALEX*.

For the X-ray count-to-flux conversion a thermal model with $kT = 1$ keV and $N_{\mathrm{H}} = 10^{20}\,\mathrm{cm^{-2}}$ is assumed. The higher temperature with respect to the 10-pc sample reflects the younger age and the larger column density the larger distance of TWA. Individual distances were used for the conversion of fluxes to luminosities.

The spectral types were converted to effective temperature using the scale of Luhman (1999) that was devised for pre-main-sequence stars with gravities in between those of dwarfs and of giants. We estimated the bolometric luminosity and stellar radii of the TWA stars from the Baraffe et al. (1998) models assuming an age of 10 Myr. Following the procedure described in Section 3.4, we have computed and subtracted the photospheric contribution to the *GALEX* fluxes for the TWA sample. Consistent with the younger age of TWA with respect to the 10-pc sample we use the DUSTY models with $\log g = 4.0$. As in the case of the 10-pc sample, the *FUV* emission can be entirely ascribed to the chromospheric excess. Less than 5 per cent of the *NUV* emission of TWA M dwarfs comes from the photosphere.

4.6.2 Results

Findeisen, Hillenbrand & Soderblom (2011) have examined the age evolution of *GALEX* UV magnitude for a sample of G stars from various clusters and associations covering ∼10 to ∼600 Myr. In Fig. 13 we show a $UV - J$ versus $J - K$ diagram for the 10-pc sample and the TWA sample to be compared to fig. 7 of Findeisen et al. (2011). We confirm the result of these authors that younger stars have bluer $UV - J$ colour at the same $J - K$ and we add more detail to it. In particular, as can be seen in Fig. 13, for the same range of $J - K$ the majority of M dwarfs from the 10-pc sample have much redder $NUV - J$ colour than the oldest sample (Hyades cluster) analysed by Findeisen et al. (2011). This is likely to be attributed to the older age of the 10-pc sample with respect to the Hyades. As far as the *FUV* is concerned, as stated by Findeisen et al. (2011) their data are dominated by non-detections and we could not derive the $FUV - J$ level of the Hyades from their fig. 7. Our Fig. 13 also shows that the anti-correlation in $UV - J$ versus $J - K$ that we see in the 10-pc sample is a result of the increasing *J*-band magnitude within the M dwarf sequence.

In Fig. 14 the luminosities and activity indices of the young M stars in TWA are compared to those of the M0…M3 stars of the 10-pc sample. The restriction to early-M spectral types was applied to the 10-pc sample because all but one of the UV-detected TWA stars have early M spectral types (cf. Fig. 13). The only late-M TWA member is TWA-28, detected in *NUV* and X-rays and clearly offset from the other TWA stars towards weaker activity in Fig. 14.

Evidently, for the same spectral type range the TWA and the 10-pc sample form two distinct groups in terms of UV and X-ray luminosities with TWA stars being brighter in all three energy bands. Only the three most active stars from the 10-pc sample (AU Mic, FK Aqr and Gl 569 AB; highlighted by circles in Figs 13 and 14) are located in the same area as TWA suggesting that these are young and/or extremely active stars. In fact, AU Mic is a debris disc system and a known member of the 12 Myr old β Pic moving group (Zuckerman et al. 2001; Kalas, Liu & Matthews 2004), FK Aqr (Gl 867 A) has long been known as a flare stare (Byrne 1979), and Gl 569 AB is a multiple system of only ∼100 Myr (Simon, Bender & Prato 2006). Our assumption of $\log g = 5$ is probably wrong for these stars but this does not affect the UV excess fluxes because their photospheric contribution is negligibly small (∼1 per cent).

The differences between the activity levels of TWA and the 10-pc sample persists if the activity indices are considered instead of the luminosities (Fig. 14 bottom) although the differences are smaller due to the drop of bolometric luminosity across time.

The age evolution of the luminosities in the UV and X-ray band for M0-M3 stars is displayed in Fig. 15. The vertical bars for the TWA and the 10-pc sample represent the full spread of observed values. We have omitted the only accretor in the sample of X-ray and *GALEX* detected TWA members. Linear

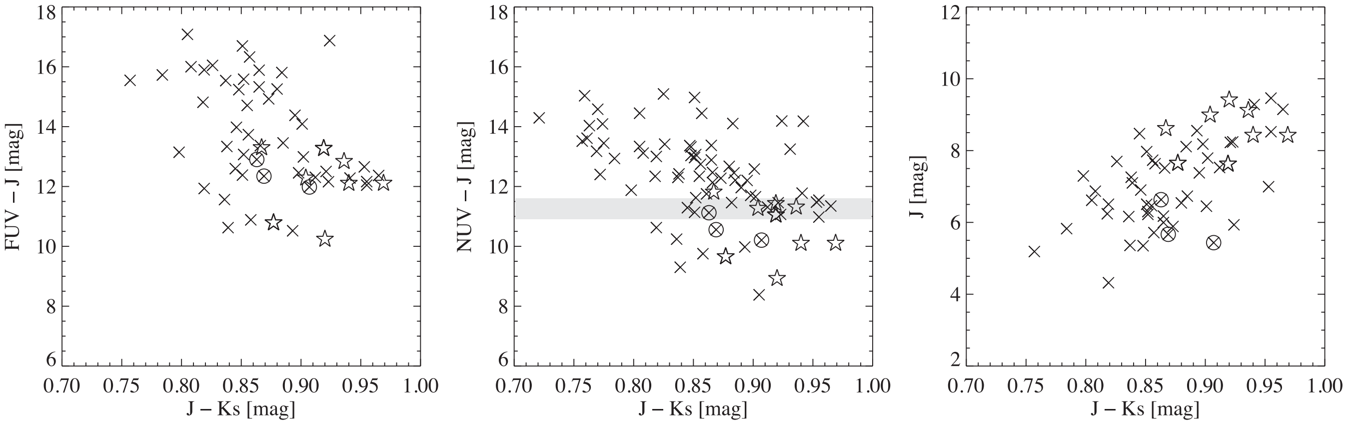

Figure 13. $UV - J$ versus $J - K_{\mathrm{s}}$ diagrams and J versus $J - K_{\mathrm{s}}$ diagram for the 10-pc sample (crosses) and the TWA sample (star symbols). Crosses surrounded by annuli highlight three young or exceptionally active stars (AU Mic, FK Aqr and Gl 569 AB) in the 10-pc sample. The grey-shaded area in the middle panel represents the range of $NUV - J$ colour observed for Hyades stars with $J > 0.7$ from Findeisen et al. (2011).

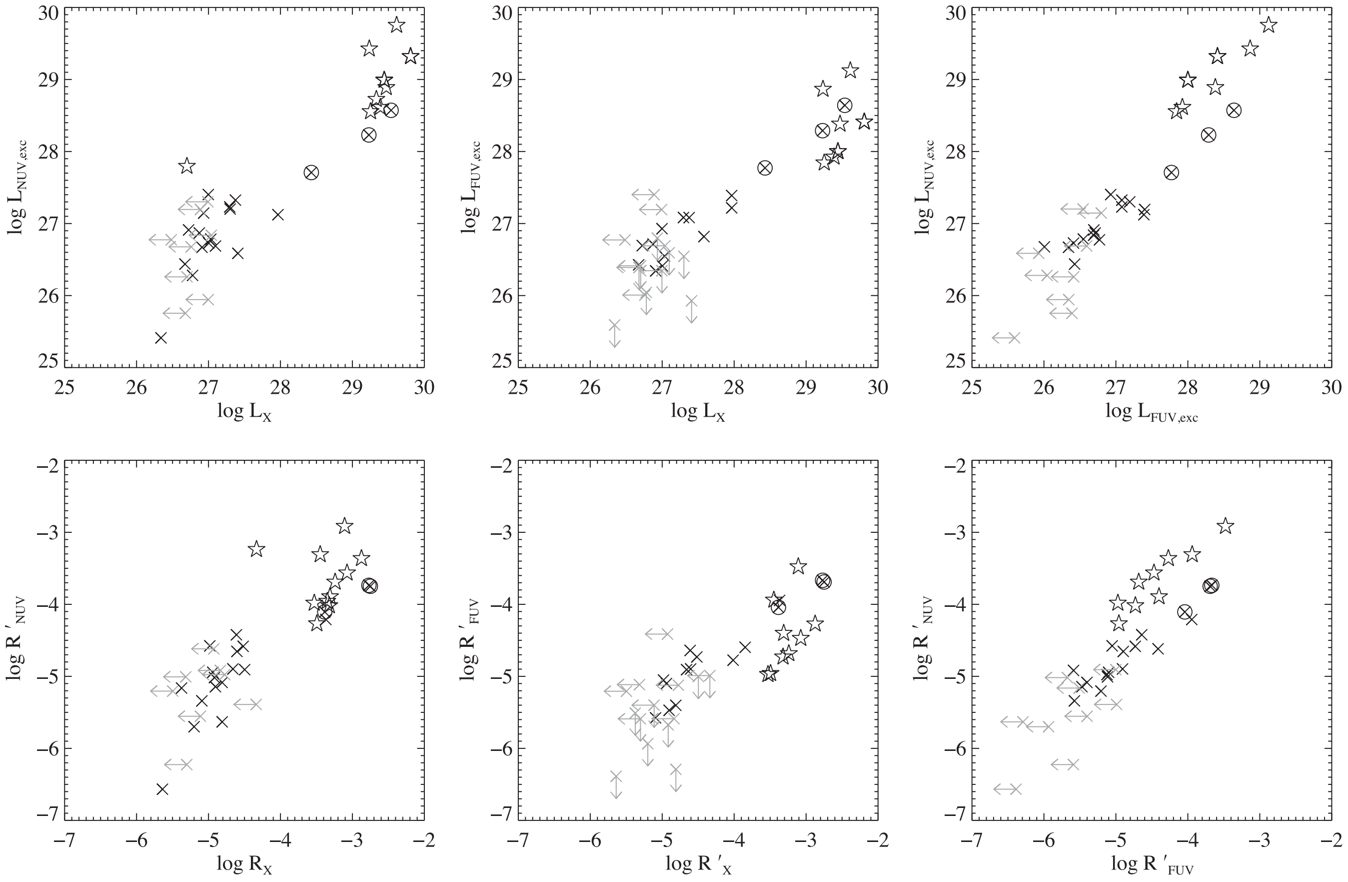

Figure 14. X-ray versus UV luminosity and activity index for M0…M3 stars from the 10-pc sample (crosses) and stars in the same spectral type range in TWA (star symbols). The three young stars AU Mic, FK Aqr and Gl 569 AB in the 10-pc sample are highlighted with annuli surrounding the plotting symbol. Upper limits are shown in grey.

regression fits in log–log form to the four data points are shown for each of the three energy bands. We have derived slopes of $\beta_{\rm X} = -1.10 \pm 0.02$, $\beta_{NUV} = -0.79 \pm 0.05$ and $\beta_{NUV} = -0.84 \pm 0.08$. Similar plots for the surface flux and activity index versus age show larger scatter of the data points especially within the TWA sample. This may be related to differences in radii within the TWA group that are not taken into account in our analysis.

5 SUMMARY AND CONCLUSIONS

Hα, UV and X-ray emission are complementary indicators of magnetic activity probing the chromosphere, transition region and corona of late-type stars. We have quantified the emissions in these wavebands for a well-defined sample of nearby M dwarfs capitalizing on recent comprehensive catalogues for Hα emission

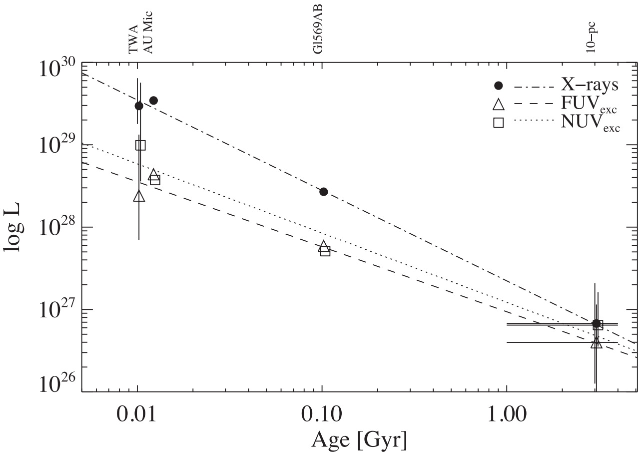

Figure 15. Age evolution of UV and X-ray luminosity for M0–M3 stars from the TWA and the 10-pc sample. The lines represent regression fits to the three activity diagnostics.

and – partly unexplored – archival data from *GALEX*, *ROSAT* and *XMM–Newton*.

We present a catalogue of Hα, *NUV*, *FUV* and X-ray fluxes for 159 M dwarfs within 10 pc of the Sun, together with the stellar parameters used to derive the fractional flux in each of the four bands with respect to the bolometric flux, the so-called activity indices. This sample has an estimated completeness of ~90 per cent.

We have subtracted the photospheric contribution to the UV fluxes of all stars with the help of synthetic model spectra. A result of this analysis is that there are no M dwarfs in the 10-pc sample without a chromospheric contribution to the *NUV* and *FUV* emission. While generally the emission in the *GALEX* bands is dominated by the chromosphere there is a trend towards increasing photospheric contribution for earlier M spectral types reflecting the shift of the stellar SED towards bluer wavelengths. The UV fluxes used throughout this paper for comparison to the Hα and X-ray emission regard only the chromospheric excess remaining after the photospheric subtraction.

As a result of the limitations of the available instrumentation, up to the present day UV spectra are available for very few M dwarfs (see references in Section 1). In particular, the faint continuum has been difficult to assess. We found from a comparison of historical records of the Mg II λ2800 Å doublet with *GALEX*/*NUV* fluxes that this line can contribute about one-third to the *NUV* emission of M dwarfs.

We have shown that with increasing activity level (measured by the X-ray flux) the relative contribution of UV emission shifts from the *NUV* to the *FUV*. Considering that stronger X-ray emitters have higher plasma temperatures (Güdel 2004), this is qualitatively consistent with the shape of the thermal bremsstrahlung continuum that increases towards shorter wavelengths for high temperatures (see Redfield et al. 2002). We recall here that the *NUV* band is dominated by chromospheric emission lines while the *FUV* band comprises many transition region emission lines. In this simplistic view, the observed dependence of $(FUV - NUV)_{\rm exc}$ on X-ray flux indicates that higher (X-ray) activity is related to a stronger enhancement of emission in the transition region with respect to the chromosphere. This is in agreement with the higher formation temperature of the *FUV* transition region lines ($T > 10^5$ K) with respect to the *NUV* emission.

We have examined flux–flux relations between Hα, *NUV*, *FUV* and X-ray emission. The tightest correlation is observed for *FUV* versus *NUV*. As *GALEX* observes simultaneously in both bands, while the X-ray and Hα observations are non-contemporaneous, this may indicate that the spread in the other relations is variability scatter. On the other hand, by comparing the fluxes for stars with more than one measurement of a given activity diagnostic (UV or X-rays) we have demonstrated that long-term variability is not an important factor for the average activity level. Therefore, the scatter in the flux–flux relations seems to represent an intrinsic range of physical conditions between the chromosphere and corona of M dwarfs. While variability in general plays a minor role in this sample, in individual cases it can be important. Comparing *GALEX* fluxes with published *HST* fluxes for two planet host stars we found one order of magnitude differences likely produced by flaring.

MD89 have studied the relation between Mg II flux and X-ray flux for M dwarfs observed with *IUE*, *EXOSAT* and *Einstein*. They found that the emission in these two observables is correlated for dMe stars while it is not correlated for dM stars. We have separated the 10-pc sample into Hα emitters (dMe) and stars with upper limit to the Hα flux (dM) and examined the flux–flux relations between UV and X-ray emission. For the 10-pc sample the trend towards larger scatter for the dM stars is confirmed but they are generally located on the extension of the flux–flux relation of dMe stars. In particular, several dM stars do show X-ray and/or chromospheric UV emission making the definition of dM as 'non-active' versus dMe as 'active' questionable. A similar conclusion was drawn by Walkowicz, Johns-Krull & Hawley (2008) who found substantial UV and X-ray flux in a number of M dwarfs without Hα emission.

For X-rays versus Hα the power-law slope for the flux–flux relation of the 10-pc sample is slightly steeper than the results of Stelzer et al. (2012) for a sample of M dwarfs that comprised also late-M spectral types. The ultracool sample from Stelzer et al. (2012) is likely biased towards strongly active objects. However, Stelzer et al. (2012) constructed their $F_{\rm surf,\,X}$ versus $F_{\rm surf,\,H\alpha}$ relation using the faintest measured flux level in case of several epochs of data for a given object. Therefore, their steeper slope may indicate a change of X-ray-to-Hα flux ratio in the low-activity regime. The upper limits of the 10-pc sample are not sensitive enough to test this hypothesis.

Despite the fact that we have exploited the most sensitive available observations for this sample of nearby M dwarfs, a substantial number of objects (30–40 per cent) remain undetected in the *FUV* and X-ray regime. The sensitivity limit may be responsible for the increase in the lower envelope of the values for the activity index in the X-ray band with increasing $T_{\rm eff}$. The largest spread of the activity indices is observed at spectral type ~ M4 where the range of rotation rates is largest. We have computed the average values of the activity indices for the subsample of fast rotators ($v \sin i >$ 5 km s^{-1}). While there are clear signs for saturation in Hα and X-rays, the scatter of the data points for fast rotators in the *NUV* and *FUV* range is large. Comparing the fractional flux output of X-rays, *FUV*, *NUV* and Hα we find an increase with energy for the four diagnostics. This trend was already noted by Hawley et al. (1996) who found $\log{(L_{\rm x}/L_{\rm H\alpha})} \sim 0.5$ in a smaller volume-limited sample. For the 10-pc sample the saturation levels for X-rays and Hα differ by nearly one order of magnitude.

Finally, to study the age evolution of the activity in M dwarfs we have analysed the UV and X-ray emission of a young comparison sample composed of the M stars from the TWA. These stars are by about a factor of 100 younger than the stars from the 10-pc sample yet accretion has stopped in the majority of them such that the observed emission can be attributed to magnetic activity. We found that between ~10 Myr and few Gyr the X-ray, *FUV* and

NUV luminosities drop by almost three orders of magnitude. A small group of young M dwarfs in the 10-pc sample bridges the gap between the luminosities of the TWA stars and the bulk of the field M dwarfs indicating that the decrease in activity with age is a continuous process. We have calculated the slopes of the age decay for the X-ray, *FUV* and *NUV* luminosities. Sanz-Forcada et al. (2011) have calculated the age–luminosity relation in the EUV band ($100 - 920$ Å) for a sample of planet host stars with spectral types F-K. They found a somewhat steeper slope than we do for the UV and X-rays bands bracketing the EUV. As the stars in our 10-pc sample and possibly also those in the TWA have an unknown age spread that we did not take into account, we do not give weight to the absolute values of our slopes. However, we can state that the age decay of the luminosity of M dwarfs is steeper for the X-ray band than for the *NUV* and *FUV*. This is similar to analogous studies on solar analogues (G stars) (Ribas et al. 2005; Claire et al. 2012).

ACKNOWLEDGEMENTS

BS would like to thank J.Sanz-Forcada and C.Cecchi-Pestellini for helpful conversations, and A. Reiners for providing the table with optical spectroscopic measurements before its official availability. We appreciate the input of an anonymous referee. This work is based on archival data from the *GALEX*, *XMM–Newton* and *ROSAT* space missions. Partial financial support from ASI is acknowledged.

REFERENCES

Adelman-McCarthy J. K. et al., 2009, VizieR Online Data Catalog, 2294, 0
Allard F., Hauschildt P. H., Alexander D. R., Tamanai A., Schweitzer A., 2001, ApJ, 556, 357
Baraffe I., Chabrier G., Allard F., Hauschildt P. H., 1998, A&A, 337, 403
Bayo A., Rodrigo C., Barrado Y Navascués D., Solano E., Gutiérrez R., Morales-Calderón M., Allard F., 2008, A&A, 492, 277
Bessell M. S., 1991, AJ, 101, 662
Bianchi L., 2009, Astrophys. Space Sci., 320, 11
Bianchi L., Efremova B., Herald J., Girardi L., Zabot A., Marigo P., Martin C., 2011, MNRAS, 411, 2770
Bochanski J. J., Hawley S. L., Covey K. R., West A. A., Reid I. N., Golimowski D. A., Ivezić Ž., 2010, AJ, 139, 2679
Browne S. E., Welsh B. Y., Wheatley J., 2009, PASP, 121, 450
Buccino A. P., Lemarchand G. A., Mauas P. J. D., 2007, Icarus, 192, 582
Byrne P. B., 1979, MNRAS, 187, 153
Byrne P. B., Butler C. J., Andrews A. D., 1980, Irish Astron. J., 14, 219
Cecchi-Pestellini C., Ciaravella A., Micela G., Penz T., 2009, A&A, 496, 863
Claire M. W., Sheets J., Cohen M., Ribas I., Meadows V. S., Catling D. C., 2012, ApJ, 757, 95
Cutri R. M. et al., 2003, 2MASS All Sky Catalog of point sources. The IRSA 2MASS All-Sky Point Source Catalog, NASA/IPAC Infrared Science Archive. http://irsa.ipac.caltech.edu/applications/Gator/
Doyle J. G., 1989, A&A, 218, 195
Doyle J. G., 1996, A&A, 307, L45
Findeisen K., Hillenbrand L., Soderblom D., 2011, AJ, 142, 23
France K., Linsky J. L., Tian F., Froning C. S., Roberge A., 2012, ApJ, 750, L32
France K. et al., 2013, ApJ, 763, 149
Gliese W., Jahreiss H., 1995, VizieR Online Data Catalog, 5070, 0
Güdel M., 2004, A&AR, 12, 71
Hawley S. L., Gizis J. E., Reid I. N., 1996, AJ, 112, 2799
Hawley S. L. et al., 2003, ApJ, 597, 535
Hawley S. L., Walkowicz L. M., Allred J. C., Valenti J. A., 2007, PASP, 119, 67
Høg E. et al., 2000, A&A, 355, L27
Isobe T., Feigelson E. D., Akritas M. G., Babu G. J., 1990, ApJ, 364, 104
Jardine M., Unruh Y. C., 1999, A&A, 346, 883
Johnson H. L., 1966, ARA&A, 4, 193
Kahn S. M., Mason K. O., Bowyer C. S., Linsky J. L., Haisch B. M., White N. E., Pravdo S. H., 1979, ApJ, 234, L107
Kalas P., Liu M. C., Matthews B. C., 2004, Sci, 303, 1990
Kasting J. F., Whitmire D. P., Reynolds R. T., 1993, Icarus, 101, 108
Koen C., Kilkenny D., van Wyk F., Marang F., 2010, MNRAS, 403, 1949
Lammer H., Selsis F., Ribas I., Guinan E. F., Bauer S. J., Weiss W. W., 2003, ApJ, 598, L121
Lecavelier Des Etangs A., 2007, A&A, 461, 1185
Lépine S., Gaidos E., 2011, AJ, 142, 138 (LG11)
Lepine S., Hilton E., Mann A., Wilde M., Rojas-Ayala B., Cruz K., Gaidos E., 2012, preprint (arXiv 1206.5991)
Looper D. L., Burgasser A. J., Kirkpatrick J. D., Swift B. J., 2007, ApJ, 669, L97
Looper D. L., Bochanski J. J., Burgasser A. J., Mohanty S., Mamajek E. E., Faherty J. K., West A. A., Pitts M. A., 2010a, AJ, 140, 1486
Looper D. L. et al., 2010b, ApJ, 714, 45
Luhman K. L., 1999, ApJ, 525, 466
Mamajek E. E., 2005, ApJ, 634, 1385
Marino A., Micela G., Peres G., 2000, A&A, 353, 177
Martin D. C. et al., 2005, ApJ, 619, L1
Martínez-Arnáiz R., López-Santiago J., Crespo-Chacón I., Montes D., 2011, MNRAS, 414, 2629
Mathioudakis M., Doyle J. G., 1989, A&A, 224, 179 (MD89)
Mohanty S., Basri G., 2003, ApJ, 583, 451
Monet D. G. et al., 2003, AJ, 125, 984
Neuhäuser R., Sterzik M. F., Schmitt J. H. M. M., Wichmann R., Krautter J., 1995, A&A, 297, 391
Oranje B. J., Zwaan C., Middelkoop F., 1982, A&A, 110, 30
Osten R. A., Hawley S. L., Allred J., Johns-Krull C. M., Brown A., Harper G. M., 2006, ApJ, 647, 1349
Pagano I., Linsky J. L., Carkner L., Robinson R. D., Woodgate B., Timothy G., 2000, ApJ, 532, 497
Penz T., Micela G., 2008, A&A, 479, 579
Perryman M. A. C., in ESA, eds., 1997, ESA Special Publication, Vol. 1200, The HIPPARCOS and TYCHO Catalogues. Astrometric and Photometric Star Catalogues Derived from the ESA HIPPARCOS Space Astrometry Mission. ESA, Noordwijk
Redfield S., Linsky J. L., Ake T. B., Ayres T. R., Dupree A. K., Robinson R. D., Wood B. E., Young P. R., 2002, ApJ, 581, 626
Reid I. N., Hawley S. L., Gizis J. E., 1995, AJ, 110, 1838
Reid I. N., Cruz K. L., Allen P. R., 2007, AJ, 133, 2825
Reiners A., Joshi N., Goldman B., 2012, AJ, 143, 93
Ribas I., Guinan E. F., Güdel M., Audard M., 2005, ApJ, 622, 680
Robinson R. D. et al., 2005, ApJ, 633, 447
Rodriguez D. R., Bessell M. S., Zuckerman B., Kastner J. H., 2011, ApJ, 727, 62
Rojas-Ayala B., Covey K. R., Muirhead P. S., Lloyd J. P., 2012, ApJ, 748, 93
Sanz-Forcada J., Micela G., Ribas I., Pollock A. M. T., Eiroa C., Velasco A., Solano E., García-Álvarez D., 2011, A&A, 532, A6
Schmitt J. H. M. M., Rosso C., 1988, A&A, 191, 99
Scholz R.-D., Irwin M., Schweitzer A., Ibata R., 1999, A&A, 345, L55
Schrijver C. J., Rutten R. G. M., 1987, A&A, 177, 143
Segura A., Kasting J. F., Meadows V., Cohen M., Scalo J., Crisp D., Butler R. A. H., Tinetti G., 2005, Astrobiology, 5, 706
Shkolnik E. L., Liu M. C., Reid I. N., Dupuy T., Weinberger A. J., 2011, ApJ, 727, 6
Simon M., Bender C., Prato L., 2006, ApJ, 644, 1183
Smith D. S., Scalo J., Wheeler J. C., 2004, Icarus, 171, 229
Stelzer B., Neuhäuser R., 2001, A&A, 377, 538
Stelzer B. et al., 2012, A&A, 537, A94
Tarter J. C. et al., 2007, Astrobiology, 7, 30
Taylor M. B., 2005, in Shopbell P., Britton M., Ebert R., eds, ASP Conf. Ser. Vol. 347, Astronomical Data Analysis Software and Systems XIV, Astron. Soc. Pac., San Francisco, p. 29

Tian F., Kasting J. F., Liu H.-L., Roble R. G., 2008, J. Geophys. Res. (Planets), 113, 5008
Torres C. A. O., Quast G. R., da Silva L., de La Reza R., Melo C. H. F., Sterzik M., 2006, A&A, 460, 695
van Leeuwen F., 2007, A&A, 474, 653
Vilhu O., 1984, A&A, 133, 117
Vilhu O., Walter F. M., 1987, ApJ, 321, 958
Walkowicz L. M., Johns-Krull C. M., Hawley S. L., 2008, ApJ, 677, 593
Watson M. G. et al., 2009, A&A, 493, 339
Welsh B. Y. et al., 2006, A&A, 458, 921
Welsh B. Y. et al., 2007, ApJS, 173, 673
Zuckerman B., Song I., Bessell M. S., Webb R. A., 2001, ApJ, 562, L87

SUPPORTING INFORMATION

Additional Supporting Information may be found in the online version of this article:

Table 1. Stellar parameters for 10-pc M dwarf sample.
Table 2. Observed *NUV*, *FUV* and X-ray fluxes for 10-pc sample. Flux units are erg cm^{-2} s^{-1}. Lower and upper values for the fluxes derived from the uncertainties are given in brackets (http://mnras.oxfordjournals.org/lookup/suppl/doi:10.1093/mnras/stt225/-/ DC1).

This paper has been typeset from a TEX/LATEX file prepared by the author.